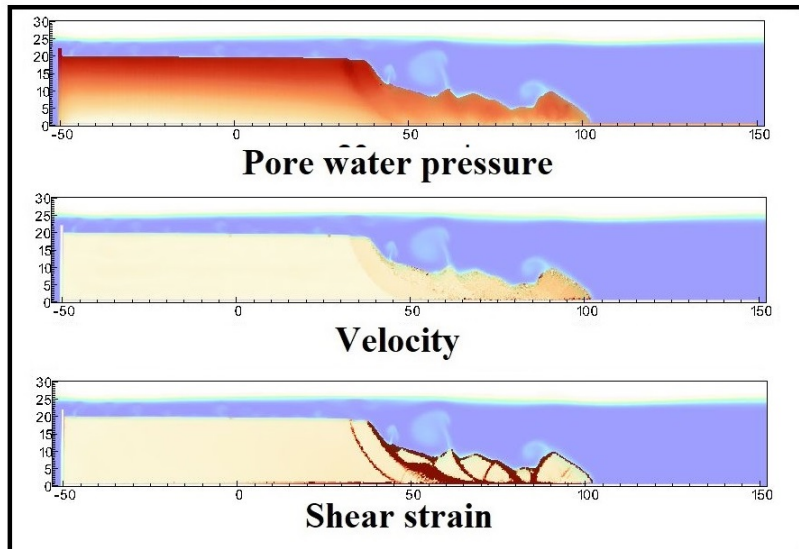


- 1 Graphical Abstract
- 2 MPMICE: A hybrid MPM-CFD model for simulating coupled problems in porous media. Application to earthquake-induced submarine landslides
- 3 Quoc Anh Tran, Gustav Grimstad, Seyed Ali Ghoreishian Amiri



**Application to earthquake-induced submarine landslide**

<sub>6</sub> Highlights

<sub>7</sub> **MPMICE: A hybrid MPM-CFD model for simulating coupled prob-**  
<sub>8</sub> **lems in porous media. Application to earthquake-induced subma-**  
<sub>9</sub> **rine landslides**

<sub>10</sub> Quoc Anh Tran, Gustav Grimstad, Seyed Ali Ghoreishian Amiri

- <sub>11</sub> • MPMICE is introduced for multiphase flow in porous media.
- <sub>12</sub> • Material Point method allows to model large deformation of non-isothermal
- <sub>13</sub> porous media.
- <sub>14</sub> • ICE (compressible multi-material CFD formulation) allows stabilizing
- <sub>15</sub> pore water pressure and turbulent flow.
- <sub>16</sub> • MPMICE is validated and apply to simulate the earthquake-induced
- <sub>17</sub> submarine landslide.

<sup>18</sup> MPMICE: A hybrid MPM-CFD model for simulating  
<sup>19</sup> coupled problems in porous media. Application to  
<sup>20</sup> earthquake-induced submarine landslides

<sup>21</sup> Quoc Anh Tran<sup>a</sup>, Gustav Grimstad<sup>a</sup>, Seyed Ali Ghoreishian Amiri<sup>a</sup>

<sup>a</sup>*Norwegian University of Science and Technology, , Trondheim, 7034, Norway*

---

<sup>22</sup> **Abstract**

<sup>23</sup> In this paper, we describe a soil-fluid-structure interaction model that com-  
<sup>24</sup> bines soil mechanics (saturated sediments), fluid mechanics (seawater or air),  
<sup>25</sup> and solid mechanics (structures). The formulation combines the Material  
<sup>26</sup> Point Method, which models large deformation of the porous media and the  
<sup>27</sup> structure, with the Implicit Continuous-fluid Eulerian, which models com-  
<sup>28</sup> plex fluid flows. We validate the model and simulate the whole process of  
<sup>29</sup> earthquake-induced submarine landslides. We show that this model captures  
<sup>30</sup> complex interactions between saturated sediment, seawater, and structure,  
<sup>31</sup> so we can use the model to estimate the impact of potential submarine land-  
<sup>32</sup> slides on offshore structures.

<sup>33</sup> *Keywords:*

<sup>34</sup> Material Point Method, MPMICE, submarine landslide.

---

<b>35</b>	<b>Contents</b>	
<b>36</b>	<b>Nomenclature</b>	<b>4</b>
<b>37</b>	<b>Introduction</b>	<b>6</b>
<b>38</b>	<b>Theory and formulation</b>	<b>8</b>
39	Assumptions . . . . .	8
40	Governing equations . . . . .	9
41	Constitutive soil model . . . . .	11
42	Turbulent model . . . . .	12
43	Frictional force for soil-structure interaction . . . . .	12
44	Momentum and Energy exchange model . . . . .	13
45	Solving momentum and energy exchange with an implicit solver	14
46	Equation of state for fluid phases . . . . .	16
<b>47</b>	<b>Numerical implementation</b>	<b>17</b>
48	Interpolation from Solid Particle to Grid . . . . .	18
49	Compute equation of state for fluid phase . . . . .	19
50	Compute faced-centered velocity . . . . .	19
51	Compute faced-centered temperature . . . . .	20
52	Compute fluid pressure (implicit scheme) . . . . .	21
53	Compute viscous shear stress term of the fluid phase . . . . .	21
54	Compute nodal internal temperature of the solid phase . . . . .	21
55	Compute and integrate acceleration of the solid phase . . . . .	22
56	Compute Lagrangian value (mass, momentum and energy) . . . . .	22
57	Compute Lagrangian specific volume of the fluid phase . . . . .	24
58	Compute advection term and advance in time . . . . .	24
59	Interpolate from cell to node of the solid phase . . . . .	25
60	Update the particle variables . . . . .	25
<b>61</b>	<b>Numerical examples</b>	<b>26</b>
62	Fluid Flow through isothermal porous media . . . . .	26
63	Isothermal consolidation . . . . .	27
64	Thermal induced cavity flow . . . . .	28
65	Underwater debris flow . . . . .	29
66	Earthquake-induced submarine landslides . . . . .	33
<b>67</b>	<b>Conclusions</b>	<b>37</b>

68	<b>Acknowledgements</b>	38
69	<b>Appendix: Equation derivation</b>	38
70	Evolution of porosity . . . . .	38
71	Momentum conservation . . . . .	39
72	Energy conservation . . . . .	40
73	Advanced Fluid Pressure . . . . .	41
74	Momentum and Energy exchange with an implicit solver . . . . .	42

<sup>75</sup> **Nomenclature**

**General variables**

<u>Variable</u>	<u>Dimensions</u>	<u>Description</u>
$V$	$[L^3]$	Representative volume
$n$		Porosity
$\sigma$	$[ML^{-1}t^{-2}]$	Total stress tensor
$\Delta t$	$[t]$	Time increment
$\mathbf{b}$	$[ML^1t^{-2}]$	Body force
$c_v$	$[L^2t^{-2}T^{-1}]$	Constant volume specific heat
$f_d$	$[MLt^{-2}]$	Drag forces in momentum exchange term
$f^{int}$	$[MLt^{-2}]$	Internal forces
$f^{ext}$	$[MLt^{-2}]$	External forces
$q_{fs}$	$[MLt^{-2}]$	Heat exchange term
$S$		Weighting function
$\nabla S$		Gradient of weighting function

<sup>76</sup>

**Solid phase**

<u>Variable</u>	<u>Dimensions</u>	<u>Description</u>
$m_s$	$[M]$	Solid mass
$\rho_s$	$[ML^{-3}]$	Solid density
$\phi_s$		Solid volume fraction
$\bar{\rho}_s$	$[ML^{-3}]$	Bulk Solid density
$\mathbf{x}_s$	$[L]$	Solid Position vector
$\mathbf{U}_s$	$[Lt^{-1}]$	Solid Velocity vector
$\mathbf{a}_s$	$[Lt^{-2}]$	Solid Acceleration vector
$\sigma'$	$[ML^{-1}t^{-2}]$	Effective Stress tensor
$\epsilon_s$		Strain tensor
$e_s$	$[L^2t^{-2}]$	Solid Internal energy per unit mass
$T_s$	$[T]$	Solid Temperature
$\mathbf{F}_s$		Solid Deformation gradient
$V_s$	$[L^3]$	Solid Volume

<sup>77</sup>

### Fluid phase

<u>Variable</u>	<u>Dimensions</u>	<u>Description</u>
$m_f$	[M]	Fluid mass
$\rho_f$	[ML <sup>-3</sup> ]	Fluid density
$\phi_f$		Fluid volume fraction
$\bar{\rho}_f$	[ML <sup>-3</sup> ]	Bulk Fluid density
$\mathbf{U}_f$	[Lt <sup>-1</sup> ]	Fluid Velocity vector
$\boldsymbol{\sigma}_f$	[ML <sup>-1</sup> t <sup>-2</sup> ]	Fluid stress tensor
$p_f$	[ML <sup>-1</sup> t <sup>-2</sup> ]	Fluid isotropic pressure
$\boldsymbol{\tau}_f$	[ML <sup>-1</sup> t <sup>-2</sup> ]	Fluid shear stress tensor
$e_f$	[L <sup>2</sup> t <sup>-2</sup> ]	Fluid Internal energy per unit mass
$T_f$	[T]	Fluid Temperature
$v_f$	[L <sup>3</sup> /M]	Fluid Specific volume $\frac{1}{\rho_f}$
$\alpha_f$	[1/T]	Thermal expansion
$\mu$	[ML <sup>-1</sup> t <sup>-1</sup> ]	Fluid viscosity
$V_f$	[L <sup>3</sup> ]	Fluid Volume

### Superscript

<u>Variable</u>	<u>Dimensions</u>	<u>Description</u>
$n$		Current time step
$L$		Lagrangian values
$n + 1$		Next time step

### Subscript

$c$	Cell-centered quantity
$p$	Particle quantity
$i$	Node quantity
$FC$	Face-centered quantity
$L, R$	Left and Right cell faces

78     **Introduction**

79     Many geological natural processes and their interactions with man-made  
80     structures are influenced by soil-fluid-structure interactions. The prediction  
81     of these processes requires a tool that can capture complex interactions  
82     between soil, fluid, and structure, such as the process of submarine land-  
83     slides. Indeed, The offshore infrastructure as well as coastal communities  
84     may be vulnerable to submarine landslides. Submarine landslides contain  
85     three stages: triggering, failure, and post-failure. Erosion or earthquakes can  
86     trigger slope failures in the first stage. Following the failure, sediments move  
87     quickly after the post-failure stage. In other words, solid-like sediments will  
88     behave like a fluid after failure. This phase transition makes the simulation  
89     of submarine landslides a challenging task.

90  
91     Due to this phase transition, submarine landslide can be modeled by ei-  
92     ther the Computational Fluid Dynamics (CFD) or the particle-based meth-  
93     ods. For simulating submarine slides, CFD methods solve governing equa-  
94     tions in a full-Eulerian framework [1, 2, 3, 4] with interface capturing tech-  
95     niques. While CFD can handle complex flows (such as turbulent flows), it  
96     cannot account for the triggering mechanism of submarine landslides because  
97     it is not straightforward to consider 'soil constitutive laws' of sediment ma-  
98     terials in the Eulerian framework. In contrast, particle-based methods can  
99     overcome this problem by using the Lagrangian framework. These meth-  
100   ods have been extensively used to simulate landslides, like Material Point  
101   Method (MPM) [5], Smooth Particle Hydro Dynamics [6], Particle Finite  
102   Element Method [7], or Coupled Eulerian Lagrangian Method [8]. For sim-  
103   plicity, these simulations adopt total stress analysis which neglects the pore  
104   pressure development which is key factor triggering slope failures.

105  
106   Recent developments in particle-based methods model the coupling of  
107   fluid flows in porous media by sets of Lagrangian particles. For the MPM  
108   family, it is the double-point MPM ([9, 10, 11]) where fluid particles and  
109   solid particles are overlapped in a single computational grid. Even if fluid  
110   flows are considered, particle-based methods have numerical instability in  
111   modeling the fluid flow, which requires additional numerical treatments such  
112   as the B-bar method [9], null-space filter [12], or least square approximation  
113   [13, 14]. Indeed, CFD is a more optimal option for complex fluid flows  
114   especially dealing with large distortions of continuum fluid media. Therefore,

115 it could be ideal to combine the CFD with particle-based methods. More than  
 116 50 particle-based methods have been developed to solve large deformations  
 117 of solids over the last two decades [15], but the MPM appears to be the  
 118 best candidate for coupling with the CFD. Because MPM incorporates a  
 119 stationary mesh during computation, just like CFD. As such, both MPM  
 120 and CFD can be coupled naturally in a unified computational mesh.



*Figure 1: Interaction between soil-fluid-structure*

121

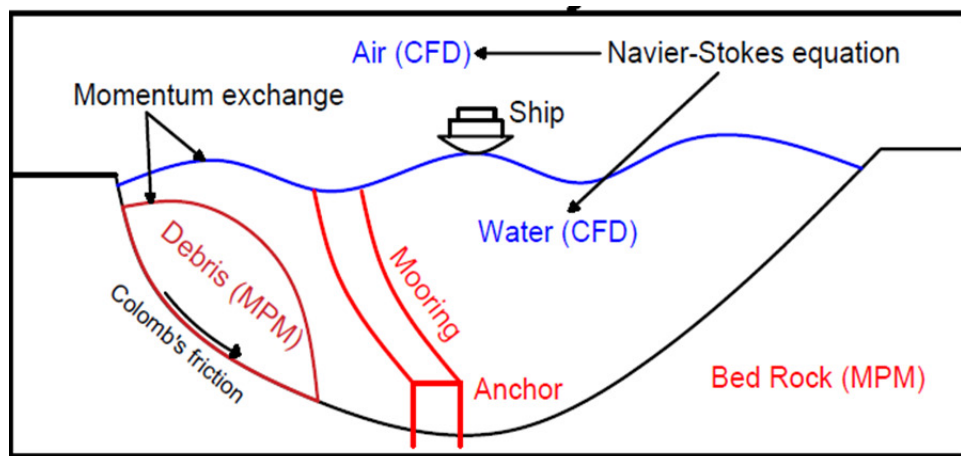


*Figure 2: Coupling of soil-water-structure interaction using MPMICE*

122 A numerical method for simulating soil-fluid-structure interaction (Figure  
123 1) involving large deformations, is presented in this work in order to simu-  
124 late the interaction between sediment (soil), seawater (fluid) and offshore  
125 structures (structure) namely MPMICE (Figure 2). In the MPMICE, the  
126 Material Point Method (MPM) is coupled with the Implicit Continuous Eu-  
127 lerian (ICE). The MPM method is a particle method that allows the porous  
128 soil to undergo arbitrary distortions. The ICE method, on the other hand,  
129 is a conservative finite volume technique with all state variables located at  
130 the cell center (temperature, velocity, mass, pressure). An initial technical  
131 report [16] at Los Alamos National Laboratory provided the theoretical and  
132 algorithmic foundation for the MPMICE, followed by the MPMICE devel-  
133 opment and implementation in the high-performance Uintah computational  
134 framework for simulating fluid-structure interactions [17]. This paper pri-  
135 marily contributes further to the development of the MPMICE for analyzing  
136 the **soil**-fluid-structure interaction, since sediment should be considered as a  
137 porous media (soil) and not as a solid to capture the evolution of the pore  
138 water pressure. Baumgarten et al. [18] made the first attempt at coupling  
139 the Finite Volume Method with the MPM for the simulation of soil-fluid  
140 interaction. In contrast to the mentioned work, we use implicit time integra-  
141 tion for the multi phase flows instead of explicit time integration for the  
142 single-phase flow.

### 143 **Theory and formulation**

144 This section lay out the theoretical framework for the MPMICE model.  
145 We use the common notation of the continuum mechanics with vector and  
146 tensor denoted simply by using bold font and scalar denoted by using normal  
147 font. The notation are shown in Nomenclature.

### 148 *Assumptions*

149 The following assumptions are made for the MPMICE model.

- 150 1. Solid phases (MPM) are described in a Lagrangian formulation while  
151 fluid phases (ICE) are described in an Eulerian formulation in the  
152 framework of continuum mechanics and mixture theory.
- 153 2. Solid grains are incompressible while the fluid phases are compressible.  
154 Solid's thermal expansion is negligible.
- 155 3. There is no mass exchange between solid and fluid phases.
- 156 4. Terzaghi's effective stress is valid.

157 *Governing equations*

158 A representative element volume  $\Omega$  is decomposed by two domains: solid  
159 domains  $\Omega_s$  and fluid domains  $\Omega_f$ . Then, all domains are homogenized  
160 into two overlapping continua. Considering the volume fraction of solid  
161  $\phi_s = \Omega_s/\Omega$  and fluid  $\phi_f = \Omega_f/\Omega$  with the true (or Eulerian) porosity  
162  $n = \sum \phi_f$  of the representative element volume, the average density of solid  
163 and fluid phases are defined as:

164

$$\bar{\rho}_s = \phi_s \rho_s, \quad \bar{\rho}_f = \phi_f \rho_f \quad (1)$$

165 The mass of solid and fluid phases are:

166

$$m_s = \int_{\Omega_s} \rho_s dV = \bar{\rho}_s V, \quad m_f = \int_{\Omega_f} \rho_f dV = \bar{\rho}_f V \quad (2)$$

167 Reviewing the Terzaghi's effective stress concept for the saturated porous  
168 media, the total stress  $\boldsymbol{\sigma}$  is calculated by:

169

$$\boldsymbol{\sigma} = \boldsymbol{\sigma}' - p_f \mathbf{I} \quad (3)$$

170 The balance equations are derived based on the mixture theory. The rep-  
171 resentative thermodynamic state of the fluid phases are given by the vector  
172  $[m_f, \mathbf{U}_f, e_f, T_f, v_f]$  which are mass, velocity, internal energy, temperature,  
173 specific volume. The representative state of the solid phases are given by the  
174 vector  $[m_s, \mathbf{U}_s, e_s, T_s, \boldsymbol{\sigma}', p_f]$  which are mass, velocity, internal energy, temper-  
175 ature, effective stress and pore water pressure. The derivation is presented  
176 in detail in the Appendix.

177

---

178 Mass Conservation

179 The mass balance equations for both fluid (e.g., water, air) and solid phases  
180 are:

181

$$\frac{1}{V} \frac{\partial m_f}{\partial t} + \nabla \cdot (m_f \mathbf{U}_f) = 0, \quad \frac{1}{V} \frac{D_s m_s}{Dt} = 0 \quad (4)$$

182 Solving the mass balance equation leads to:

$$\frac{D_s n}{Dt} = \phi_s \nabla \cdot \mathbf{U}_s \quad (5)$$

183

---

184 Momentum Conservation

<sup>185</sup> The momentum balance equation for the fluid phases (e.g., water, air) are:

<sup>186</sup>

$$\frac{1}{V} \left[ \frac{\partial(m_f \mathbf{U}_f)}{\partial t} + \nabla \cdot (m_f \mathbf{U}_f \mathbf{U}_f) \right] = -\phi_f \nabla p_f + \nabla \cdot \boldsymbol{\tau}_f + \bar{\rho}_f \mathbf{b} + \sum \mathbf{f}_d \quad (6)$$

<sup>187</sup> The momentum balance equation for the solid phases are:

<sup>188</sup>

$$\frac{1}{V} \frac{D_s(m_s \mathbf{U}_s)}{Dt} = \nabla \cdot (\boldsymbol{\sigma}') - \phi_s \nabla p_f + \bar{\rho}_s \mathbf{b} + \sum \mathbf{f}_{fric} - \sum \mathbf{f}_d \quad (7)$$

<sup>189</sup>

---

### <sup>190</sup> Energy Conservation

<sup>191</sup> The internal energy balance equation for the fluid phases (e.g., water, air)  
<sup>192</sup> are:

$$\frac{1}{V} \left[ \frac{\partial(m_f e_f)}{\partial t} + \nabla \cdot (m_f e_f \mathbf{U}_f) \right] = -\bar{\rho}_f p_f \frac{D_f v_f}{Dt} + \boldsymbol{\tau}_f : \nabla \mathbf{U}_f + \nabla \cdot \mathbf{q}_f + \sum q_{sf} \quad (8)$$

<sup>193</sup> The internal energy balance equation for the solid phase is:

$$\frac{m_s}{V} c_v \frac{D_s(T_s)}{Dt} = \boldsymbol{\sigma}' : \frac{D_s(\boldsymbol{\epsilon}_s^p)}{Dt} + \nabla \cdot \mathbf{q}_s - \sum q_{sf} \quad (9)$$

<sup>194</sup> where  $c_v$  is the specific heat at constant volume of the solid materials.

<sup>195</sup>

---

<sup>196</sup> Closing the systems of equations, the following additional models are needed:

<sup>197</sup> (1) A constitutive equation to describe the stress - strain behaviour of solid  
<sup>198</sup> phase (computing effective stress  $\boldsymbol{\sigma}'$ ).

<sup>199</sup> (2) Optional turbulent model to compute the viscous shear stress  $\boldsymbol{\tau}_f$ .

<sup>200</sup> (3) Frictional forces  $\mathbf{f}_{fric}$  for the contact for soil-structure interaction be-  
<sup>201</sup> tween solid/porous materials with the friction coefficient  $\mu_{fric}$ .

<sup>202</sup> (4) Exchange momentum models (computing drag force  $\mathbf{f}_d$ ) for interaction  
<sup>203</sup> between materials.

<sup>204</sup> (5) Energy exchange models (computing temerature exhangre term  $q_{sf}$ ) for  
<sup>205</sup> interaction between materials.

<sup>206</sup> (6) An equation of state to establish relations between thermodynamics vari-  
<sup>207</sup> ables of each fluid materials  $[P_f, \bar{\rho}_f, v_f, T_f, e_f]$ .

<sup>208</sup> Four thermodynamic relations for the equation of states are:

$$\begin{aligned} e_f &= e_f(T_f, v_f) \\ P_f &= P_f(T_f, v_f) \\ \phi_f &= v_f \bar{\rho}_f \\ 0 &= n - \sum_{f=1}^{N_f} v_f \bar{\rho}_f \end{aligned} \quad (10)$$

<sup>209</sup> *Constitutive soil model*

<sup>210</sup> As a result of the explicit MPM formulation, we can derive the consti-  
<sup>211</sup> tutive law in the updated Lagrangian framework of "small strain - large  
<sup>212</sup> deformation". Therefore, the rotation of the particles (representative ele-  
<sup>213</sup> ment volume) is manipulated by rotating the Cauchy stress tensor. First,  
<sup>214</sup> the deformation gradient is decomposed into the polar rotation tensor  $\mathbf{R}_s^{n+1}$   
<sup>215</sup> and stretch tensor  $\mathbf{V}_s^{n+1}$  as

$$\mathbf{F}_s^{n+1} = \mathbf{V}_s^{n+1} \mathbf{R}_s^{n+1} \quad (11)$$

<sup>216</sup> Then, before calling the constitutive model, the stress and strain rate tensor  
<sup>217</sup> are rotated to the reference configuration as

$$\boldsymbol{\sigma}'^{n*} = (\mathbf{R}_s^{n+1})^T \boldsymbol{\sigma}'^{n*} \mathbf{R}_s^{n+1} \quad (12)$$

$$\delta\boldsymbol{\epsilon}^{n*} = (\mathbf{R}_s^{n+1})^T \delta\boldsymbol{\epsilon}_s^{n*} \mathbf{R}_s^{n+1} \quad (13)$$

<sup>219</sup> Using the constitutive model with the input tensors  $\boldsymbol{\sigma}'^{n*}, \delta\boldsymbol{\epsilon}^{n*}$  to compute  
<sup>220</sup> the Cauchy stress tensor at the advanced time step  $\boldsymbol{\sigma}'^{n+1*}$  then rotating it  
<sup>221</sup> back to current configuration

$$\boldsymbol{\sigma}'^{n+1} = \mathbf{R}_s^{n+1} \boldsymbol{\sigma}'^{n+1*} (\mathbf{R}_s^{n+1})^T \quad (14)$$

<sup>222</sup> In this paper, we adopt the hyper-elastic Neo Hookean model for the structure  
<sup>223</sup> materials and additionally Mohr-Coulomb failure criteria for the soil (porous  
<sup>224</sup> media) materials. The Cauchy stress of the hyper-elastic Neo Hookean model  
<sup>225</sup> can be written as:

$$\boldsymbol{\sigma}' = \frac{\lambda \ln(J)}{J} + \frac{\mu}{J} (\mathbf{F} \mathbf{F}^T - \mathbf{J}) \quad (15)$$

<sup>226</sup> where  $\lambda$  and  $\mu$  are bulk and shear modulus ad  $J$  is the determinant of the  
<sup>227</sup> deformation gradient  $\mathbf{F}$ . And the yield function  $f$  and flow potentials  $g$  of

<sup>228</sup> the Mohr-Coulomb can be written as:

$$\begin{aligned} f &= \sigma'_1 - \sigma'_3 - 2c' \cos(\phi') - (\sigma'_1 + \sigma'_3) \sin(\phi') \\ g &= \sigma'_1 - \sigma'_3 - 2c' \cos(\psi') - (\sigma'_1 + \sigma'_3) \sin(\psi') \end{aligned} \quad (16)$$

<sup>229</sup> where the  $c'$ ,  $\phi'$  and  $\psi'$  are cohesion and friction angle and dilation angle.  $\sigma'_1$   
<sup>230</sup> and  $\sigma'_3$  are maximum and minimum principal stress.

<sup>231</sup> *Turbulent model*

<sup>232</sup> The turbulent effect is modelled using a statistical approach namely large-  
<sup>233</sup> eddy simulation. In this approach, the micro-scale turbulent influence in the  
<sup>234</sup> dynamics of the macro-scale motion is computed through simple models like  
<sup>235</sup> Smagorinsky model. In the Smagorinsky model, the residual stress tensor is:

$$\tau_{ij} = 2\mu_{eff}(\bar{S}_{ij} - \frac{1}{3}\delta_{ij}\bar{S}_{kk}) + \frac{1}{3}\delta_{ij}\tau_{kk} \quad (17)$$

<sup>236</sup> where the strain rate tensor is given by

$$\bar{S}_{ij} = \frac{1}{2}(\frac{\delta \bar{U}_i}{\delta x_j} + \frac{\delta \bar{U}_j}{\delta x_i}) \quad (18)$$

<sup>237</sup> and the effective viscosity is sum of molecular viscosity and turbulent viscosity  
<sup>238</sup>  $\mu_{eff} = \mu + \mu_t$  in which the turbulent viscosity  $\mu_t$  is calculated by

$$\mu_t = (C_s \Delta)^2 \sqrt{2\bar{S}_{ij}\bar{S}_{ij}} \quad (19)$$

<sup>239</sup> where  $C_s$  is the Smagorinsky constant with the value of 0.1 and  $\Delta = \sqrt[3]{dxdydz}$   
<sup>240</sup> is the grid size that defines the subgrid length scale.

<sup>241</sup> *Frictional force for soil-structure interaction*

<sup>242</sup> MPMICE includes a contact law for the interaction between soil and  
<sup>243</sup> structure using the first Coulomb friction contact for MPM presented by  
<sup>244</sup> Bardenhagen et al. ([19]). The magnitude of the friction force at the contact  
<sup>245</sup> depends on the friction coefficient  $\mu_{fric}$  and the normal force  $\mathbf{f}_{norm}$  computed  
<sup>246</sup> from the projection of the contact force in the normal direction.

$$\mathbf{f}_{fric} = \mu_{fric} \mathbf{f}_{norm} \quad (20)$$

247 The contact determines whether the soil is sliding or sticking to the structure  
 248 by comparing the friction force with the sticking force  $\mathbf{f}_{stick}$  computed from  
 249 the projection of the contact force in the tangent direction:

$$\begin{aligned} \text{if } \mathbf{f}_{fric} \geq \mathbf{f}_{stick} & \text{ no sliding} \\ \text{if } \mathbf{f}_{fric} < \mathbf{f}_{stick} & \text{ sliding occurs} \end{aligned} \quad (21)$$

250 Frictional sliding between solid materials also generates dissipation and the  
 251 work rate generated from the sliding can be calculated as:

$$\Delta W_{friction} = \mathbf{f}_{fric} d \quad (22)$$

252 where  $d$  is the sliding distance which can be computed based on the sliding  
 253 velocity between two materials.

254 *Momentum and Energy exchange model*

255 Currently, the energy exchange coefficient  $H_{sf}$  is assumed to be constant  
 256 for the sake of simplicity. Then the energy exchange can be written as:

$$q_{sf} = H_{sf}(T_f - T_s) \quad (23)$$

257 On the other hand, the drag force can be calculated as:

$$f_d = K(\mathbf{U}_s - \mathbf{U}_f) \quad (24)$$

258 For the momentum exchange between fluid flows and porous media, we as-  
 259 sume that the drag force  $\mathbf{f}_d$  depends on the average grain size of the grains  
 260  $D_p$ , the porosity  $n$ , the fluid viscosity  $\mu_f$ , and is proportional to the relative  
 261 velocities of soil grains and fluid  $(\mathbf{U}_s - \mathbf{U}_f)$ . Based on recent investigation  
 262 of CFD simulations of fluid flow around mono- and bi-disperse packing of  
 263 spheres for  $0.1 < \phi_s < 0.6$  and  $Re < 1000$  [20]. The drag force is given by:

$$\mathbf{f}_d = \frac{18\phi_s(1-\phi_s)\mu_f}{D_p^2} F(\phi_s, Re)(\mathbf{U}_s - \mathbf{U}_f) \quad (25)$$

264 where Reynolds number  $Re$  are computed as:

$$Re = \frac{n\rho_f D_p}{\mu_f} \|(\mathbf{U}_s - \mathbf{U}_f)\| \quad (26)$$

<sup>266</sup> The function  $F(\phi_s, Re)$  can be calculated as:

$$F(\phi_s, Re) = F(\phi_s, 0) + \frac{0.413Re}{24(1 - \phi_s)^2} \left( \frac{(1 - \phi_s)^{-1} + 3\phi_s(1 - \phi_s) + 8.4Re^{-0.343}}{1 + 10^{3\phi_s}Re^{-(1+4\phi_s)/2}} \right) \quad (27)$$

<sup>267</sup> where the low Reynold coefficient  $F(\phi_s, Re \rightarrow 0)$  is:

$$F(\phi_s, 0) = \frac{10\phi_s}{(1 - \phi_s)^2} + (1 - \phi_s)^2(1 + 1.5\sqrt{\phi_s}) \quad (28)$$

<sup>268</sup> When validating the model with analytical solution, it requires to know the  
<sup>269</sup> hydraulic conductivity  $K$ . In such case, we convert the equation (29) to  
<sup>270</sup> Kozeny-Carman formula by assuming  $F(\phi_s, Re) = 10\phi_s/(1 - \phi_s)^2$ , leading to

$$\mathbf{f}_d = \frac{180\phi_s^2\mu_f}{D_p^2(1 - \phi_s)} (\mathbf{U}_s - \mathbf{U}_f) \quad (29)$$

<sup>271</sup> Then, the draging force following the Darcy law is given by:

$$\mathbf{f}_d = \frac{n^2\mu_f}{\kappa} (\mathbf{U}_s - \mathbf{U}_f) \quad (30)$$

<sup>272</sup> where  $\kappa$  being intrinsic permeability of soil which can be written as:

$$\kappa = \frac{K\mu_f}{\rho_f g} \quad (31)$$

<sup>273</sup> As such, the hydraulic conductivity will be expressed as:

$$K = \frac{D_p^2(1 - \phi_s)^3}{180\phi_s^2\mu_f} \rho_f g \quad (32)$$

<sup>274</sup> *Solving momentum and energy exchange with an implicit solver*

<sup>275</sup> The derivation of the implicit integration for the momentum exchange is  
<sup>276</sup> presented in the Appendix's section 'Momentum and energy exchange with  
<sup>277</sup> an implicit solver'. The linear equations for multi phases i,j=1:N has the  
<sup>278</sup> form:

$$\begin{vmatrix} (1 + \beta_{ij}) & -\beta_{ij} \\ -\beta_{ji} & (1 + \beta_{ji}) \end{vmatrix} \begin{vmatrix} \Delta \mathbf{U}_i \\ \Delta \mathbf{U}_j \end{vmatrix} = \begin{vmatrix} \beta_{ij}(\mathbf{U}_i^* - \mathbf{U}_j^*) \\ \beta_{ji}(\mathbf{U}_i^* - \mathbf{U}_j^*) \end{vmatrix}$$

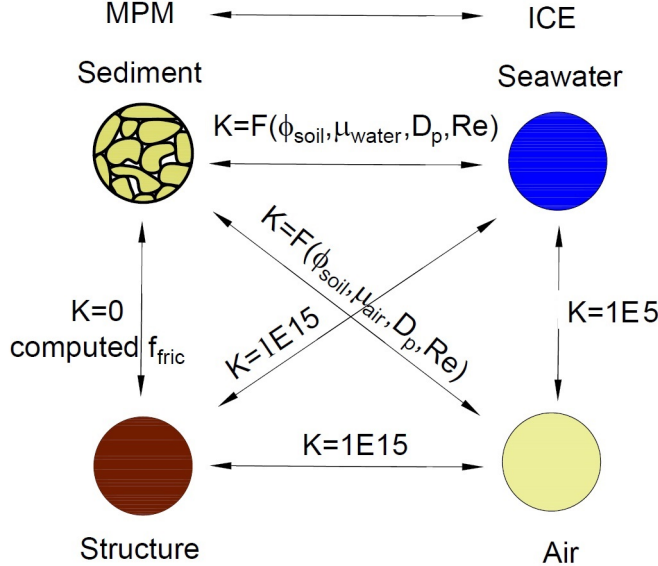


Figure 3: Momentum exchange coefficient between materials

279 where the intermediate velocity for fluid phases  $f=1:N_f$  and for solid/porous  
280 phases  $s=1:N_s$  can be calculated by

$$\begin{aligned} U_f^* &= U_f^n + \Delta t \left( -\frac{\nabla P_f^{n+1}}{\rho_f^n} + \frac{\nabla \cdot \tau_f^n}{\bar{\rho}_f^n} + \mathbf{b} \right) \\ U_s^* &= U_s^n + \Delta t \left( \frac{\nabla \cdot \sigma'^n}{\bar{\rho}_s^n} - \frac{\nabla P_f^{n+1}}{\rho_s} + \mathbf{b} \right) \end{aligned} \quad (33)$$

281 Also, the momentum exchange coefficient can be computed at every time  
282 step as  $\beta_{12} = K/\bar{\rho}_f^n$  and  $\beta_{21} = K/\bar{\rho}_s^n$  with the coefficient depending on the  
283 different type of interactions (see Figure 3) as for example:

284

- 285 1. The drag force is set to zero in soil-structure interactions, and instead  
286 the frictional force is computed.  
287 2. As a result of fluid-structure interaction, the momentum exchange coef-  
288 ficient should be extremely high (1E15) when the solid material points  
289 are considered to be zero-porosity/zero-permeability.  
290 3. In the case of soil-fluid interaction, the drag force is calculated using  
291 the equation (29). Considering that air has a much lower viscosity than

water, its drag force is much lower than the drag force of water in a pore.

4. A momentum exchange coefficient of 1E5 is applied between multiphase flows. This value is far higher than reality [21], but it is necessary to have enough numerical stability to conduct simulations in the numerical example.

Similar approach applied for the energy exchange term leading to:

$$\begin{vmatrix} (1 + \eta_{ij}) & -\eta_{ij} \\ -\eta_{ji} & (1 + \eta_{ji}) \end{vmatrix} \begin{vmatrix} \Delta T_i \\ \Delta T_j \end{vmatrix} = \begin{vmatrix} \eta_{ij}(T_i^n - T_j^n) \\ \eta_{ji}(T_j^n - T_i^n) \end{vmatrix}$$

with  $\eta$  is the energy exchange coefficient.

300

### 301 *Equation of state for fluid phases*

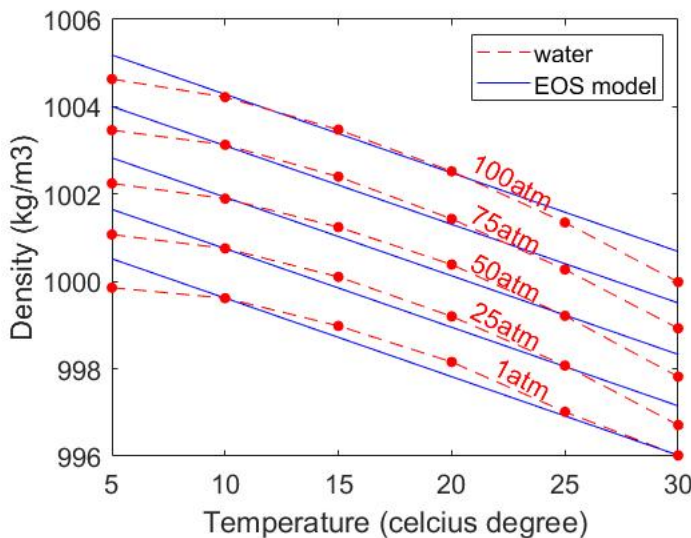


Figure 4: Equation of state of water

The equation of state establishes relations between thermodynamics variables  $[P_f, \rho_f, T_f]$ . The choice of the equation of state depends on the types of the fluid materials. For example, for the air, it is possible to assume the equation of state for the perfect gas which obeys:

$$P_f = \rho_f R T_f \quad (34)$$

306 where  $R$  is the gas constant. For the water, a simple linear equation of state  
 307 is in the following form:

$$P_f = P_{ref} + K_f(\rho_f - \rho_{ref} - \alpha_f(T_f - T_{ref})) \quad (35)$$

308 where reference pressure  $P_{ref} = 1$  atm = 101325 Pa, reference temperature  
 309  $T_{ref} = 10^\circ\text{C}$ , reference density  $\rho_{ref} = 999.8 \text{ kg/m}^3$ , the bulk modulus of water  
 310  $K_f = 2 \text{ GPa}$ , and the water thermal expansion  $\alpha_f = 0.18 \text{ }^\circ\text{C}^{-1}$ . Equation  
 311 (35) matches well with the state of the water (see Figure 4).

312 **Numerical implementation**

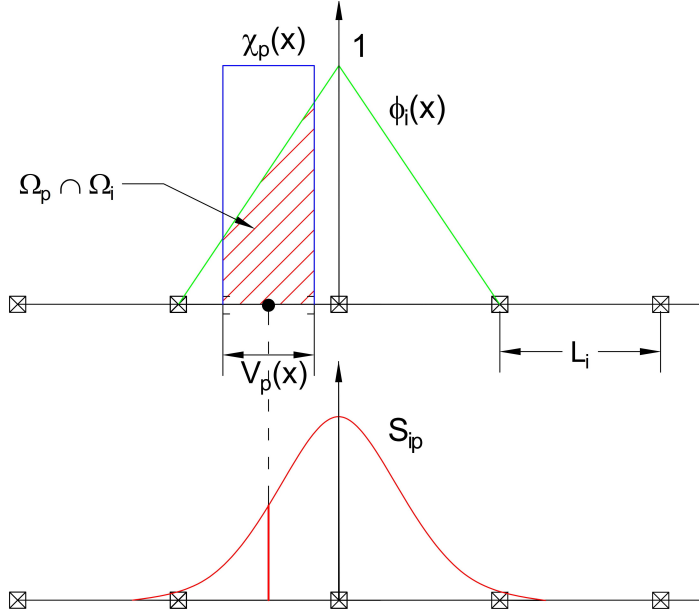


Figure 5: GIMP weighting function (red as a convolution of the linear basis shape function (green) and the characteristic function (blue))

313 The fluid phases are discretized in the grid with the state variables stored  
 314 at the centroid of the cells  $[\rho_{fc}, \mathbf{U}_{fc}, T_{fc}, v_{fc}]$  while the solid phase is dis-  
 315 cretized in the particles with the state variables  $[m_{sp}, \mathbf{U}_{sp}, T_{sp}, \boldsymbol{\sigma}'_{sp}]$ . In the  
 316 Material Point Method, we use the generalized interpolation technique [22]  
 317 using the weight function as a convolution of a grid shape function  $N_i(\mathbf{x})$  in

<sup>318</sup> a nodal domain  $\Omega_i$  and a characteristic function  $\chi_p(\mathbf{x})$  in a particle domain  
<sup>319</sup>  $\Omega_p$  with the volume  $V_p(\mathbf{x})$  as follows:

$$S_{ip} = \frac{1}{V_p} \int_{\Omega_i \cap \Omega_p} N_i(\mathbf{x}) \chi_p(\mathbf{x}) d\mathbf{x} \quad (36)$$

<sup>320</sup> where the volume  $V_p(\mathbf{x})$  of the material point p can be calculated as:

$$V_p = \int_{\Omega_p} \chi_p(\mathbf{x}) d\mathbf{x} \quad (37)$$

<sup>321</sup> The characteristic function is the Heaviside function as  $\chi_p = 1$  if  $\mathbf{x} \in \Omega_p$ ,  
<sup>322</sup> otherwise 0 (see Figure 5). For the interpolation of the centroid of the cell,  
<sup>323</sup> the linear basis function is used as:

$$S_{ci} = N_i(\mathbf{x}_c) \quad (38)$$

<sup>324</sup> The time discretization are solved using the following steps:

#### <sup>325</sup> *Interpolation from Solid Particle to Grid*

<sup>326</sup> The nodal values of the solid state (mass, velocity, temperature, volume)  
<sup>327</sup> are:

$$\begin{aligned} m_{si}^n &= \sum S_{ip} m_{sp} \\ \mathbf{U}_{si}^n &= \frac{\sum S_{ip} (m\mathbf{U})_{sp}^n}{m_{si}^n} \\ T_{si}^n &= \frac{\sum S_{ip} (mT)_{sp}^n}{m_{si}^n} \\ V_{si}^n &= \frac{\sum S_{ip} (mV)_{sp}^n}{m_{si}^n} \\ \boldsymbol{\sigma}_{si}^n &= \frac{\sum S_{ip} (\boldsymbol{\sigma}V)_{sp}^n}{V_{si}^n} \end{aligned} \quad (39)$$

<sup>328</sup> The nodal internal forces is calculated by

$$\mathbf{f}_{si}^{int,n} = - \sum \nabla S_{ip} (\boldsymbol{\sigma}'_{sp})^n V_{sp}^n \quad (40)$$

<sup>329</sup> The nodal external forces  $f_{si}^{ext,n}$  and extra momentum from contact forces  
<sup>330</sup> are computed here. The nodal velocity and nodal temperature are applied

<sup>331</sup> boundary conditions.

<sup>332</sup> Then we compute the solid cell variables as:

$$\begin{aligned} m_{sc}^n &= \sum S_{ci} m_{si} \\ \rho_{sc}^n &= \frac{m_{sc}^n}{V} \\ \mathbf{U}_{sc}^n &= \sum S_{ci} \mathbf{U}_{si}^n \\ T_{sc}^n &= \sum S_{ci} T_{si}^n \\ V_{sc}^n &= \sum S_{ci} V_{si}^n \\ \boldsymbol{\sigma}_{sc}^n &= \sum S_{ci} \boldsymbol{\sigma}_{si}^n \end{aligned} \tag{41}$$

<sup>333</sup> *Compute equation of state for fluid phase*

<sup>334</sup> Considering the total fluid material volume of a cell is:

$$V_{total} = \sum_{f=1}^{N_f} M_f v_f \tag{42}$$

<sup>335</sup> Then we need to find  $P_{eq}$  which allows each fluid materials obey their equation  
<sup>336</sup> of states  $[P_f, \rho_f, v_f, T_f, e_f]$  but also allow mass of all fluid materials to fill the  
<sup>337</sup> entire the pore volume without ongoing compression or expansion following  
<sup>338</sup> the condition:

$$0 = n - \sum_{f=1}^{N_f} v_f \bar{\rho}_f \tag{43}$$

<sup>339</sup> Then, we can use the Newton-Raphson interation to find the value of  $P_{eq}$   
<sup>340</sup> which satisfies the equation (42, 43) and each equation of states of each fluid  
<sup>341</sup> materials.

<sup>342</sup> *Compute faced-centered velocity*

<sup>343</sup> Following the derivation in the Appendix: Advanced Fluid Pressure, we  
<sup>344</sup> first compute the fluid face-centered velocity as

$$\mathbf{U}_{f,FC}^* = \frac{(\bar{\rho} \mathbf{U})_{f,FC}^n}{\bar{\rho}_{f,FC}^n} + \Delta t \left( -\frac{\nabla^{FC} P_{eq}}{\rho_{f,FC}^n} + \frac{\nabla^{FC} \cdot \boldsymbol{\tau}^n}{\bar{\rho}_{s,FC}} + \mathbf{b} \right) \tag{44}$$

<sup>346</sup> The equation (44) is discretized in three dimension (noted that  $\nabla^{FC} \cdot \boldsymbol{\tau} = 0$ ),  
<sup>347</sup> for example the discretized equation in the x direction is

$$U_{fx}^* = \frac{(\bar{\rho}U)_{fx,R}^n + (\bar{\rho}U)_{fx,L}^n}{\bar{\rho}_{fx,L}^n + \bar{\rho}_{fx,R}^n} + \Delta t \left( -\frac{2(v_{fx,L}^n v_{fx,R}^n)}{v_{fx,L}^n + v_{fx,R}^n} \frac{P_{eqx,R} - P_{eqx,L}}{\Delta x} + b_x \right) \quad (45)$$

<sup>348</sup> The face-centered solid velocity can be calculated as

$$\mathbf{U}_{s,FC}^* = \frac{(\bar{\rho}\mathbf{U})_{s,FC}^n}{\bar{\rho}_{s,FC}^n} + \Delta t \left( \frac{\nabla^{FC} \cdot \boldsymbol{\sigma}_c'^n}{\bar{\rho}_{s,FC}^n} - \frac{\nabla^{FC} P_{eq}}{\rho_s} + \mathbf{b} \right) \quad (46)$$

<sup>349</sup> The equation (46) is discretized in three dimension(noted that  $\nabla^{FC} \cdot \boldsymbol{\sigma}_{ij} = 0$   
<sup>350</sup> with  $i \neq j$ ), for example the discretized equation in the x direction is

$$U_{sx}^* = \frac{(\bar{\rho}U)_{sx,R}^n + (\bar{\rho}U)_{sx,L}^n}{\bar{\rho}_{sx,L}^n + \bar{\rho}_{sx,R}^n} + \Delta t \left( \frac{2(\sigma_{xx,R} - \sigma_{xx,L})}{(\bar{\rho}_{sx,L}^n + \bar{\rho}_{sx,R}^n)\Delta x} - \frac{P_{eqx,R} - P_{eqx,L}}{\rho_s \Delta x} + b_x \right) \quad (47)$$

<sup>351</sup> Computing the modified faced-centered velocity  $\mathbf{U}_{FC}^L$  considering the mo-  
<sup>352</sup> mentum exchange (see the Appendix: Momentum exchange with an implicit  
<sup>353</sup> solve)

$$\begin{aligned} \mathbf{U}_{f,FC}^L &= \mathbf{U}_{f,FC}^* + \Delta \mathbf{U}_{f,FC} \\ \mathbf{U}_{s,FC}^L &= \mathbf{U}_{s,FC}^* + \Delta \mathbf{U}_{s,FC} \end{aligned} \quad (48)$$

<sup>354</sup> Solving the linear equation below to obtain the increment of velocity with i,j  
<sup>355</sup> = 1 : N as:

$$\begin{vmatrix} (1 + \beta_{ij}) & -\beta_{ij} \\ -\beta_{ji} & (1 + \beta_{ji}) \end{vmatrix} \begin{vmatrix} \Delta \mathbf{U}_{i,FC} \\ \Delta \mathbf{U}_{j,FC} \end{vmatrix} = \begin{vmatrix} \beta_{ij} (\mathbf{U}_{i,FC}^* - \mathbf{U}_{j,FC}^*) \\ \beta_{ji} (\mathbf{U}_{j,FC}^* - \mathbf{U}_{i,FC}^*) \end{vmatrix}$$

### <sup>356</sup> Compute faced-centered temperature

<sup>357</sup> Similar to the velocity, the faced temperature is computed as:

$$T_{fx}^n = \frac{(\bar{\rho}T)_{fx,R}^n + (\bar{\rho}T)_{fx,L}^n}{\bar{\rho}_{fx,L}^n + \bar{\rho}_{fx,R}^n} \quad (49)$$

<sup>358</sup> Computing the modified faced-centered temperature  $T_{FC}^L$  considering the en-  
<sup>359</sup> ergy exchange (see the Appendix: Momentum and energy exchange with an  
<sup>360</sup> implicit solver)

$$\begin{aligned} T_{f,FC}^L &= T_{f,FC}^n + \Delta T_{f,FC} \\ T_{s,FC}^L &= T_{s,FC}^n + \Delta T_{s,FC} \end{aligned} \quad (50)$$

<sup>361</sup> Solving the linear equation below to obtain the increment of velocity with  $i,j$   
<sup>362</sup>  $= 1 : N$  as:

$$\begin{vmatrix} (1 + \eta_{ij}) & -\eta_{ij} \\ -\eta_{ji} & (1 + \eta_{ji}) \end{vmatrix} \begin{vmatrix} \Delta T_{i,FC} \\ \Delta T_{j,FC} \end{vmatrix} = \begin{vmatrix} \eta_{ij}(T_{i,FC}^n - T_{j,FC}^n) \\ \eta_{ji}(T_{j,FC}^n - T_{i,FC}^n) \end{vmatrix}$$

<sup>363</sup> **Compute fluid pressure (implicit scheme)**

<sup>364</sup> For single phase flow, the increment of the fluid pressure can be computed  
<sup>365</sup> as:

$$\kappa_f \frac{\Delta P}{dt} = \nabla^c \cdot \mathbf{U}_{f,FC}^{n+1} \quad (51)$$

<sup>366</sup> For multi-phase flows, the increment of the fluid pressure of the mixture can  
<sup>367</sup> be computed as:

$$\kappa \frac{\Delta P}{dt} = \sum_{f=1}^{N_f} \nabla^c \cdot (\phi_{f,FC} \mathbf{U}_{f,FC})^{n+1} \quad (52)$$

<sup>368</sup> where  $\kappa = \sum_{f=1}^{N_f} (\phi_{f,FC} \kappa_f) / \sum_{f=1}^{N_f} (\phi_{f,FC})$ . Then, the fluid pressure at cell  
<sup>369</sup> center is:

$$P_c^{n+1} = P_{eq} + \Delta P_c^n \quad (53)$$

<sup>370</sup> Finally, the faced-centered advanced fluid pressure is

$$P_{FC}^{n+1} = \left( \frac{P_{c,L}^{n+1}}{\bar{\rho}_{f,L}^n} + \frac{P_{c,R}^{n+1}}{\bar{\rho}_{f,R}^n} \right) / \left( \frac{1}{\bar{\rho}_{f,L}^n} + \frac{1}{\bar{\rho}_{f,R}^n} \right) = \left( \frac{P_{c,L}^{n+1} \bar{\rho}_{f,R}^n + P_{c,R}^{n+1} \bar{\rho}_{f,L}^n}{\bar{\rho}_{f,L}^n \bar{\rho}_{f,R}^n} \right) \quad (54)$$

<sup>371</sup> **Compute viscous shear stress term of the fluid phase**

<sup>372</sup> This part compute the viscous shear stress  $\Delta(m\mathbf{U})_{fc,\tau}$  for a single vis-  
<sup>373</sup> cous compressible Newtonian fluid and optionally shear stress induced by  
<sup>374</sup> the turbulent model.

<sup>375</sup> **Compute nodal internal temperature of the solid phase**

<sup>376</sup> The nodal internal temperature rate is computed based on the heat con-  
<sup>377</sup> duction model

$$dT_{si}^L = \frac{(\Delta W_{si}^n + \Delta W_{fric,i}^n + \nabla^i \cdot \mathbf{q}_{si}^n)}{m_{si}^n c_v} \quad (55)$$

<sup>378</sup> where  $\Delta W_{si}^n = \boldsymbol{\sigma}' : \frac{D_s(\boldsymbol{\epsilon}_s^p)}{Dt}$  is the mechanical work rate computed from the  
<sup>379</sup> constitutive model with  $\boldsymbol{\epsilon}_s^p$  is the plastic strain,  $\Delta W_{fric,i}^n$  is the work rate

380 computed from the contact law due to the frictional sliding between solid  
 381 materials. The heat flux is  $\mathbf{q}_s = \bar{\rho}_s \beta_s \nabla T_s$  with  $\beta_s$  being the thermal conductivity of the solid materials.

$$T_{si}^L = T_{si}^n + dT_{si}^L \quad (56)$$

383 *Compute and integrate acceleration of the solid phase*

384 After interpolating from material points to the nodes, the nodal acceleration  
 385 and velocity are calculate by

$$\mathbf{a}_{si}^{L-} = \frac{\mathbf{f}_{si}^{int,n} + \mathbf{f}_{si}^{ext,n}}{m_{si}^n} + \mathbf{g} \quad (57)$$

$$\mathbf{U}_{si}^{L-} = \mathbf{U}_{si}^n + \mathbf{a}_{si}^{L-} \Delta t \quad (58)$$

387 *Compute Lagrangian value (mass, momentum and energy)*

388 For the fluid phase, the linear momentum rate, the energy rate are

$$\Delta(m\mathbf{U})_{fc} = V n_c^n \nabla^c P_c^{n+1} + \Delta(m\mathbf{U})_{fc,\tau} + V \bar{\rho}_{fc}^n g \quad (59)$$

$$\Delta(me)_{fc} = V n_c^n P_c^{n+1} \nabla^c \cdot \mathbf{U}_{f,FC}^* + \nabla^c \cdot \mathbf{q}_{fc}^n \quad (60)$$

390 The Lagrangian value of the mass, linear momentum and energy of fluid  
 391 phases without momentum exchange are

$$m_{fc}^L = V \bar{\rho}_{fc}^n \quad (61)$$

$$(m\mathbf{U})_{fc}^{L-} = V \bar{\rho}_{fc}^n \mathbf{U}_{fc}^n + \Delta(m\mathbf{U})_{fc} \quad (62)$$

$$(me)_{fc}^{L-} = V \bar{\rho}_{fc}^n T_{fc}^n c_v + \Delta(me)_{fc} \quad (63)$$

394 For the solid phase, the Lagrangian value of the linear momentum and energy  
 395 of solid phase are

$$m_{sc}^L = m_{sc}^n \quad (64)$$

$$(m\mathbf{U})_{sc}^{L-} = \sum S_{ci} m_{si}^n \mathbf{U}_{si}^{L-} + V(1 - n_c^n) \nabla^c P_{fc}^{n+1} \quad (65)$$

$$(me)_{sc}^{L-} = \sum S_{ci} m_{si}^n T_{si}^L c_v \quad (66)$$

398 To consider the momentum exchange, the Lagrangian velocity is modified as

$$\begin{aligned} \mathbf{U}_{fc}^L &= \mathbf{U}_{fc}^{L-} + \Delta \mathbf{U}_{fc} \\ \mathbf{U}_{sc}^L &= \mathbf{U}_{sc}^{L-} + \Delta \mathbf{U}_{sc} \end{aligned} \quad (67)$$

<sup>399</sup> where the cell-centered intermediate velocity can be calculated by

$$\begin{aligned}\mathbf{U}_{fc}^{L-} &= \frac{(m\mathbf{U})_{fc}^{L-}}{m_{fc}^L} \\ \mathbf{U}_{sc}^{L-} &= \frac{(m\mathbf{U})_{sc}^{L-}}{m_{sc}^L}\end{aligned}\quad (68)$$

<sup>400</sup> And the increment of the velocity  $\mathbf{U}_{fc}$ ,  $\Delta\mathbf{U}_{sc}$  can be computed by solving the  
<sup>401</sup> linear equation with  $i,j = 1 : N$  as:

$$\begin{vmatrix} (1 + \beta_{ij}) & -\beta_{ij} \\ -\beta_{ji} & (1 + \beta_{ji}) \end{vmatrix} \begin{vmatrix} \Delta\mathbf{U}_{i,c} \\ \Delta\mathbf{U}_{j,c} \end{vmatrix} = \begin{vmatrix} \beta_{ij}(\mathbf{U}_{i,c}^* - \mathbf{U}_{j,c}^*) \\ \beta_{ji}(\mathbf{U}_{j,c}^* - \mathbf{U}_{i,c}^*) \end{vmatrix}$$

<sup>402</sup> To consider the energy exchange, the Lagrangian temperature is modified as

$$\begin{aligned}T_{fc}^L &= T_{fc}^{L-} + \Delta T_{fc} \\ T_{sc}^L &= T_{sc}^{L-} + \Delta T_{sc}\end{aligned}\quad (69)$$

<sup>403</sup> where the cell-centered intermediate temperature can be calculated by

$$\begin{aligned}T_{fc}^{L-} &= \frac{(mT)_{fc}^{L-}}{m_{fc}^L c_v} \\ T_{sc}^{L-} &= \frac{(mT)_{sc}^{L-}}{m_{sc}^L c_v}\end{aligned}\quad (70)$$

<sup>404</sup> And the increment of the velocity can be computed by solving the linear  
<sup>405</sup> equation with  $i,j = 1 : N$  as:

$$\begin{vmatrix} (1 + \eta_{ij}) & -\eta_{ij} \\ -\eta_{ji} & (1 + \eta_{ji}) \end{vmatrix} \begin{vmatrix} \Delta T_{i,c} \\ \Delta T_{j,c} \end{vmatrix} = \begin{vmatrix} \eta_{ij}(T_{i,c}^n - T_{j,c}^n) \\ \eta_{ji}(T_{j,c}^n - T_{i,c}^n) \end{vmatrix}$$

<sup>406</sup> Finally, we obtain the cell-centered solid acceleration and temperature rate  
<sup>407</sup> as

$$d\mathbf{U}_{sc}^L = \frac{(m\mathbf{U})_{sc}^L - (m\mathbf{U})_{sc}^n}{m_{sc}^L \Delta t} \quad (71)$$

$$dT_{sc}^L = \frac{(me)_{sc}^L - (me)_{sc}^n}{m_{sc}^L c_v \Delta t} \quad (72)$$

409    ***Compute Lagrangian specific volume of the fluid phase***

410    To compute the Lagrangian value of the specific volume of the fluid phase,  
 411    we need to compute the Lagrangian temperature rate as below

$$T_{fc}^{n+1} = \frac{(me)_{fc}^L}{m_{fc}^L c_v} \quad (73)$$

$$\frac{D_f T_{fc}}{Dt} = \frac{T_{fc}^{n+1} - T_{fc}^n}{\Delta t} \quad (74)$$

413    As such, the Lagrangian specific volume rate is:

$$\Delta(mv)_{fc} = V f_{fc}^\phi \nabla \cdot \mathbf{U} + (\phi_{fc} \alpha_{fc} \frac{D_f T_{fc}}{Dt} - f_{fc}^\phi \sum_{n=1}^N \phi_{nc} \alpha_{nc} \frac{D_n T_{nc}}{Dt}) \quad (75)$$

414    where  $f_f^\phi = (\phi_f \kappa_f) / (\sum_{n=1}^N \phi_n \kappa_n)$  and  $\mathbf{U} = \nabla \cdot (\sum_{s=1}^{N_s} \phi_{sc} \mathbf{U}_{sc} + \sum_{f=1}^{N_f} \phi_{fc} \mathbf{U}_{fc})$ .  
 415    Finally, the Lagrangian specific volume is

$$(mv)_{fc}^L = V \bar{\rho}_{f,c}^n v_{fc}^n + \Delta(mv)_{fc} \quad (76)$$

416    ***Compute advection term and advance in time***

417    The time advanced mass, linear momentum, energy and specific volume  
 418    are:

$$m_{fc}^{n+1} = m_{fc}^L - \Delta t \nabla \cdot (\bar{\rho}_{fc}^L, \mathbf{U}_{f,FC}^L) \quad (77)$$

$$(m\mathbf{U})_{fc}^{n+1} = (m\mathbf{U})_{fc}^L - \Delta t \nabla \cdot ((\bar{\rho}\mathbf{U})_{fc}^L, \mathbf{U}_{f,FC}^L) \quad (78)$$

$$(me)_{fc}^{n+1} = (me)_{fc}^L - \Delta t \nabla \cdot ((\bar{\rho}c_v T)_{fc}^L, \mathbf{U}_{f,FC}^L) \quad (79)$$

$$(mv)_{fc}^{n+1} = (mv)_{fc}^L - \Delta t \nabla \cdot ((\bar{\rho}v)_{fc}^L, \mathbf{U}_{f,FC}^L) \quad (80)$$

422    Finally, the state variables of the fluid phases of the next time step are

$$\bar{\rho}_{fc}^{n+1} = \frac{m_{fc}^{n+1}}{V} \quad (81)$$

$$\mathbf{U}_{fc}^{n+1} = \frac{(m\mathbf{U})_{fc}^{n+1}}{m_{fc}^{n+1}} \quad (82)$$

$$T_{fc}^{n+1} = \frac{(me)_{fc}^{n+1}}{m_{fc}^{n+1}} \quad (83)$$

$$v_{fc}^{n+1} = \frac{(mv)_{fc}^{n+1}}{m_{fc}^{n+1}} \quad (84)$$

426    *Interpolate from cell to node of the solid phase*

427    First we interpolate the acceleration, velocity and temperature rate to  
428    the node

$$429 \quad \mathbf{a}_{si}^n = \sum S_{ci} d\mathbf{U}_{sc}^L \quad (85)$$

$$430 \quad \mathbf{U}_{si}^{n+1} = \sum S_{ci} d\mathbf{U}_{sc}^L \Delta t \quad (86)$$

$$431 \quad dT_{si}^n = \sum S_{ci} dT_{sc}^L \quad (87)$$

432    Then the boundary condition and contact forces are applied to the nodal  
433    velocity and the acceleration is modified by

$$434 \quad \mathbf{a}_{si}^n = \frac{\mathbf{v}_{si}^{n+1} - \mathbf{v}_{si}^n}{\Delta t} \quad (88)$$

435    *Update the particle variables*

436    The state variables of the solid phase  $[\mathbf{U}_{sp}^{n+1}, \mathbf{x}_{sp}^{n+1}, \nabla \mathbf{U}_{sp}^{n+1}, T_{sp}^{n+1}, \nabla T_{sp}^{n+1}, \mathbf{F}_{sp}^{n+1}, V_{sp}^{n+1}]$   
437    (velocity, position, velocity gradient, temperature, temperature gradient, de-  
438    formation gradient, volume) are updated here

$$439 \quad \mathbf{U}_{sp}^{n+1} = \mathbf{U}_{sp}^n + \sum S_{sp} \mathbf{a}_{si}^n \Delta t \quad (89)$$

$$440 \quad \mathbf{x}_{sp}^{n+1} = \mathbf{x}_{sp}^n + \sum S_{sp} \mathbf{U}_{si}^{n+1} \Delta t \quad (90)$$

$$441 \quad \nabla \mathbf{U}_{sp}^{n+1} = \sum \nabla S_{sp} \mathbf{U}_{si}^{n+1} \quad (91)$$

$$442 \quad T_{sp}^{n+1} = T_{sp}^n + \sum S_{sp} dT_{si}^n \Delta t \quad (92)$$

$$443 \quad \nabla T_{sp}^{n+1} = \sum \nabla S_{sp} T_{sp}^n \Delta t \quad (93)$$

$$444 \quad \mathbf{F}_{sp}^{n+1} = (\mathbf{I} + \nabla \mathbf{U}_{sp}^{n+1} \Delta t) \mathbf{F}_{sp}^n \quad (94)$$

$$445 \quad V_{sp}^{n+1} = \det(\mathbf{F}_{sp}^{n+1}) V_{sp}^o \quad (95)$$

446    Finally, the effective stress  $(\boldsymbol{\sigma}')^{n+1}$  is updated from the constitutive model  
447    and the pore water pressure is interpolated from the cell as:

$$448 \quad p_f^{n+1} = \sum S_{si} P_c^{n+1} \quad (96)$$

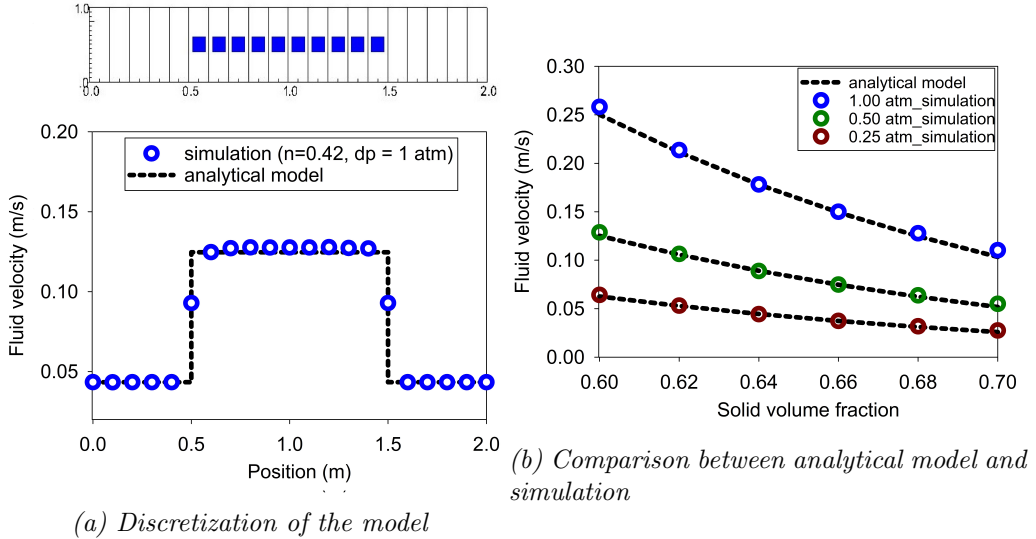


Figure 6: Numerical results of the fluid flow through isothermal porous media

#### 445 Numerical examples

446 All input files and the analytical calculations in this section are provided  
 447 in the Github repository for the reproduction of the numerical results.

448

#### 449 Fluid Flow through isothermal porous media

450 Fluid flow through porous media is important in many engineering disciplines,  
 451 like predicting water flow in soil. Fluid flow velocity in one dimension  
 452 can be calculated from the porous media's hydraulic conductivity  $K$  as:

453

$$U_f = K \frac{\Delta p_f}{L} \quad (97)$$

454 If the Carman-Kozeny formula is adopted  $F = 10\phi_s/(1 - \phi_s)^2$ , the hydraulic  
 455 conductivity will be expressed as  $K = D_p^2(1 - \phi_s)^3\rho_f g/180\phi_s^2\mu_f$ . Then, the  
 456 analytical formula of average velocity in one dimension through the porous  
 457 media is:

458

$$U_f = \frac{1}{n} \frac{D_p^2(1 - \phi_s)^3}{180\phi_s^2\mu_f} \frac{\Delta p_f}{L} \quad (98)$$

Our numerical model is validated by modeling fluid flow through a 1m long porous media. This fluid has water properties (bulk modulus is 2GPa, density is 998 kg/m<sup>3</sup> at 5 degrees Celsius and 10325 Pa (1atm) pressure, dynamic viscosity  $\mu_f$  is 1mPa s). The porous media is modeled by elastic material with Young's modulus is 10 MPa, Poisson's ratio is 0.3, and density is 2650 kg/m<sup>3</sup>. The volume fraction of porous media  $\phi_s$  is [0.6, 0.62, 0.66, 0.68, 0.7] and the average grain diameter  $d$  is 1mm. The model is discretized in 20 finite element and the porous media in 10 finite element with 1 material point per element. The pressure gradient is applied with three different value [0.25, 0.5, 1] atm. Figure 6 shows a good agreement of fluid flow prediction between the theory and the model.

470

#### 471 Isothermal consolidation

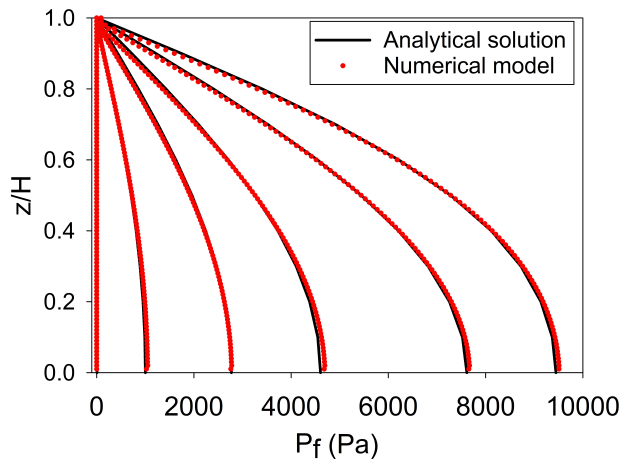


Figure 7: Comparison between analytical solution and numerical solution

A common benchmark for a fully saturated porous media is the simulation of one-dimensional consolidation. Using the Carman-Kozeny formula, the time-dependent pressure can be calculated as:

$$p_f = \sum_{m=1}^{\infty} \frac{2F_{ext}}{M} \sin\left(\frac{Mz}{H}\right) e^{-M^2 T_v} \text{ with } M = \frac{\pi}{2}(2m+1) \quad (99)$$

where the consolidation rate  $T_v = C_v t / H^2$ , the consolidation coefficient  $C_v = E_v n^3 d^2 / (180(1-n)^2 \mu)$  and the Oedometer modulus  $E_v = E(1-v)/(1+v)$ .

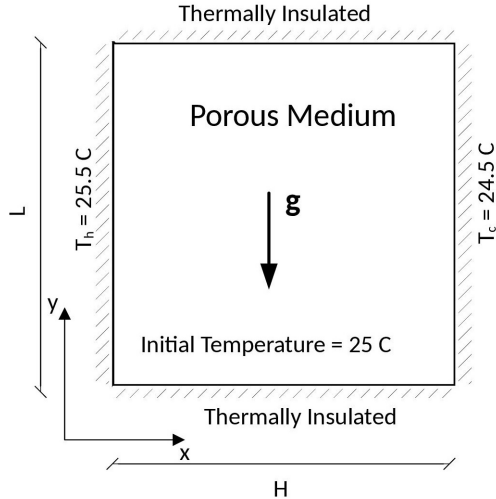


Figure 8: Model schematic [23]

477  $v)/(1-2v)$ . Our numerical model is validated by modeling the consolidation  
 478 of a 1m column. This fluid has water properties (bulk modulus is 2GPa,  
 479 density is 998 kg/m<sup>3</sup> at 5 degrees Celsius and 101325 Pa (1atm) pressure,  
 480 dynamic viscosity  $\mu$  is 1mPa s). The porous media is modeled by elastic  
 481 material with Young's modulus is 10 MPa, Poisson's ratio is 0.3, and density  
 482 is 2650 kg/m<sup>3</sup>. The volume fraction of porous media  $\phi_s$  is 0.7 which is equiv-  
 483 alent to the porosity of 0.3 and the average grain diameter  $d$  is 1mm. The  
 484 model is discretized in 100 finite element with 1 material point per element.  
 485 The external pressure applies to the top of the column is 10 kPa. Figure 7  
 486 shows a good agreement of fluid flow prediction between the theory and the  
 487 model.

488

489 *Thermal induced cavity flow*

490 Another benchmark is the thermal induced cavity flow in porous me-  
 491 dia. Temperature and velocity distributions are calculated for a square non-  
 492 deformable saturated porous media. The top and bottom walls are insulated,  
 493 and the left and right walls are at fixed temperature gradient of 1 degree.  
 494 The fluid motion at steady state are cavity flow due to the temperature in-  
 495 duced density variation.  
 496 The numerical is validated by comparing with the numerical solution of the fi-  
 497 nite element method. The fluid has water properties (bulk modulus is 2GPa,

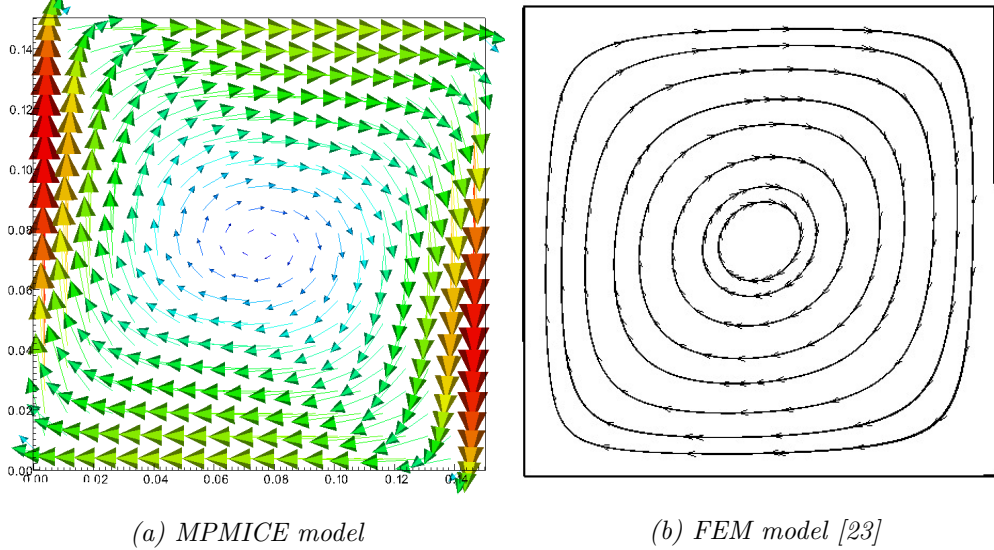


Figure 9: Comparison between MPMICE model and FEM model

density is  $998 \text{ kg/m}^3$  at 5 degrees Celsius and 10325 Pa (1atm) pressure, dynamic viscosity  $\mu$  is  $1 \text{ mPa s}$ ). The porous media is modeled by non deformable material, and density is  $2500 \text{ kg/m}^3$ . The specific heat capacity of the water and porous skeleton are  $4181 \text{ J/kg.K}$  and  $835 \text{ J/kg.K}$  respectively. The thermal conductivity of the water and porous skeleton are  $0.598 \text{ W/m.K}$  and  $0.4 \text{ W/m.K}$ . The volume fraction of porous media  $\phi_s$  is 0.6 which is equivalent to the porosity of 0.4 and the average grain diameter  $d$  is 1mm. The model is discretized in  $20 \times 20$  finite element with 4 material point per element. Figure 9 shows a good agreement of numerical results of the model compared with the numerical solution of the finite element method.

508

### 509 Underwater debris flow

510 The numerical example is validated by Rzadkiewicz et al.'s experiment  
511 on submarine debris flow [24]. During the experiment, sand in a triangular  
512 box is released and then slides along a rigid bed inclined 45 degrees under  
513 water, see Figure 10.

514 In the numerical model, the material properties are selected based on the  
515 experiment by Rzadkiewicz et al [24]. Sand has a saturated density of  $1985 \text{ kg/m}^3$   
516 and yield stress of 200 Pa. Young's modulus has little effect on debris

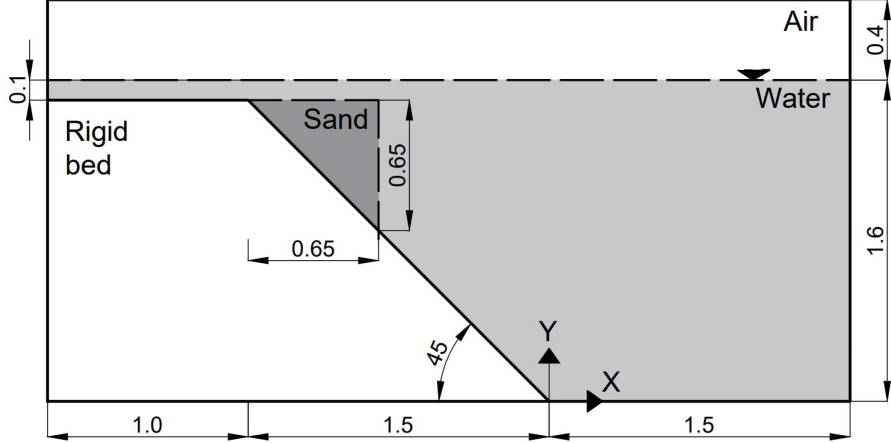


Figure 10: Model schematic

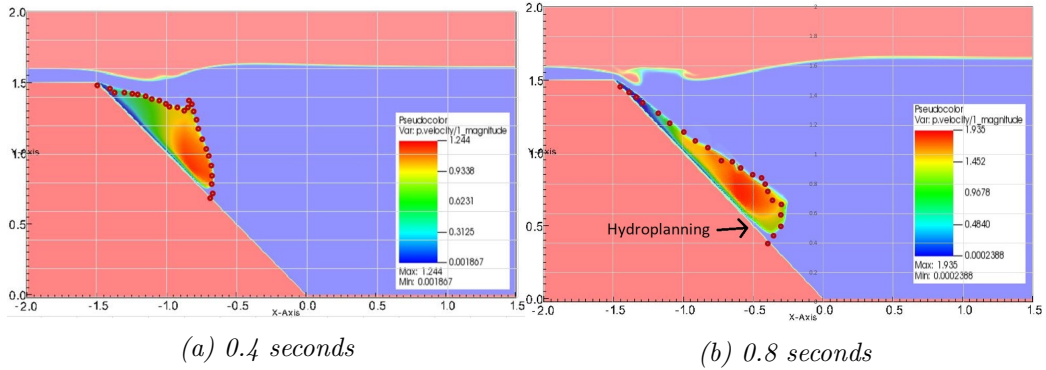


Figure 11: Simulation of underwater debris flow

517 flow run-out because of the extreme large deformation of the debris. Therefore,  
 518 we select 50 MPa Young's modulus with 0.25 Poisson's ratio. The rigid  
 519 bed is much stiffer with bulk modulus and shear modulus of  $117E^7$  Pa and  
 520  $43.8E^7$  Pa. Under gravity, the density of the water at the surface is  $999.8$   
 521  $kg/m^3$  at the pressure of 1 atm. At the top boundary, the air has a density  
 522 of  $1.17 kg/m^3$  at the atmospheric pressure of 1 atm. At 5 Celcius degrees,  
 523 air and water have viscosity of  $18.45E^{-3}$  mPa s and 1 mPa s respectively.  
 524 The numerical parameters used in this example are presented in Table 1.  
 525 On all boundary faces, the Dirichlet boundary condition is imposed for velocity  
 526 ( $u = 0$  m/s) and temperature ( $T = 5$  Celcius degrees), while the Neuman  
 527 boundary condition is imposed at the top boundary for pressure ( $dp/dx = 0$ )

Materials	Bulk modul (Pa)	Shear modul (Pa)	Density (kg/m <sup>3</sup> )	Temp (C)	Dynamic viscosity (Pa s)	Yield stress (Pa)
Water (at surface)	2.15e9	-	999.8	5	855e-6	-
Air (at top boundary)	-	-	1.177	5	18.45e-6	-
Sand (porous media)	8.33e6	20e6	1985	5	-	200
Rigid bed (solid)	117e7	43.8e7	8900	5	-	-

*Table 1: Numerical parameters for the underwater submarine debris*

528 kPa) and density ( $d\rho/dx = 0 \text{ kg/m}^3$ ). For the background mesh, there are  
 529  $700 \times 400 = 280.000$  cells. In each cell of the debris flow and rigid bed, there  
 530 are  $2 \times 2$  material points.

531 Figure 11a and 11b show snapshots of the debris flow sliding in the plane  
 532 at 0.4 s and 0.8 s. Our simulations match the computed results from Rzad-  
 533 kiewicz et al. [24]. The model also captures typical hydroplaning mechanism  
 534 of the underwater debris flow (hydroplaning means the debris flow is lifted  
 535 up and no longer in contact with the bottom layer). The elevation of the free  
 536 surface at 0.4s and 0.8s is compared between our proposed method and other  
 537 methods in Figure 12. Once again, our computed results were consistent with  
 538 both the experiment and others computational results [7]. Unlike other com-  
 539 putational models based on total stress analysis, the proposed model based  
 540 on the effective stress analysis which allows to analyze the water pressure  
 541 and temperature in the debris flow.

542 We also explore the difference between underwater debris flow and satu-  
 543 rated debris flow in terms of interacting with obstacle. Figure 13 shows the  
 544 snapshot of the simulations of underwater and saturated debris flow. The  
 545 saturated debris flow (see Figure 13a) behaves like frictional flow as grain  
 546 have contact forces with each other. On the other hand, the underwater de-  
 547bris flow (see Figure 13b) behaves like turbulent flow as grains are separated  
 548 from each other and exhibit no contact forces between grains.

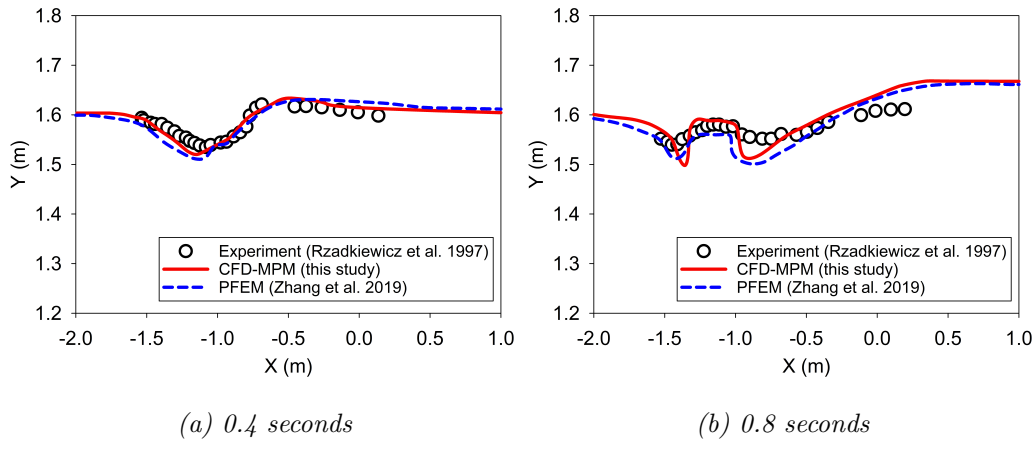


Figure 12: Simulation of underwater debris flow

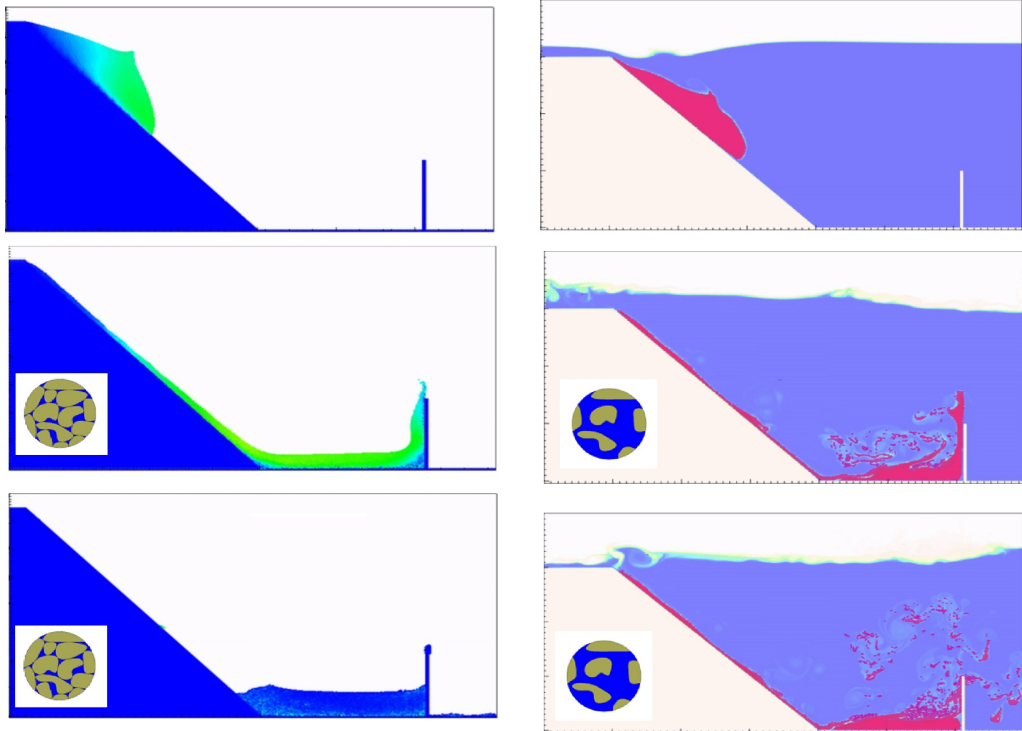


Figure 13: Simulation of underwater debris flow

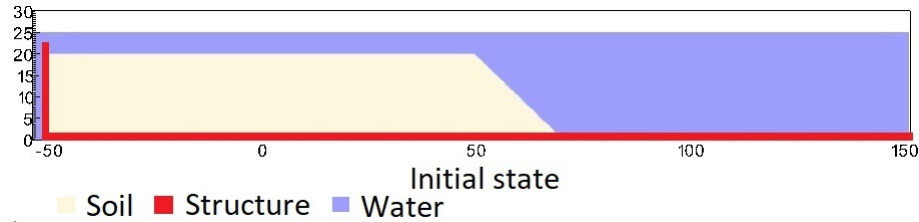
550 *Earthquake-induced submarine landslides*

Figure 14: Numerical model of the earthquake-induced submarine landslide

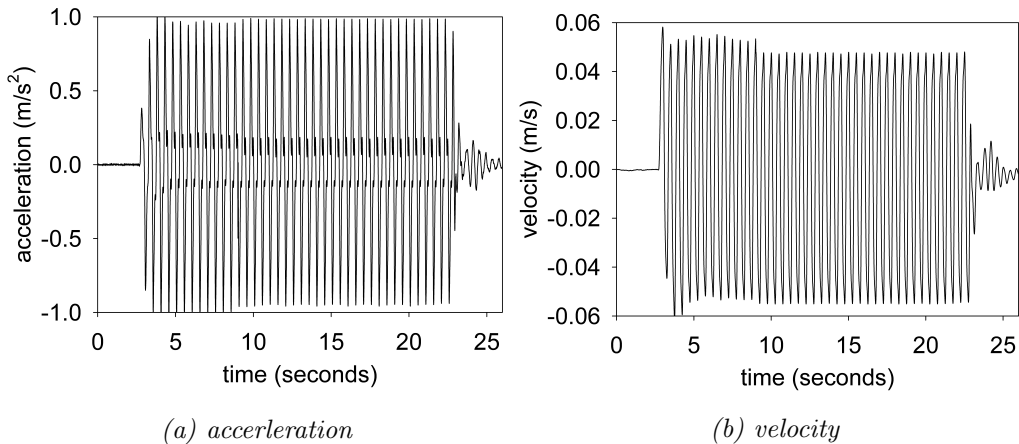


Figure 15: Ground acceleration profile, frequency of 2Hz and magnitude of 1g

551 In the final example, we perform numerical analysis of the earthquake in-  
 552 duced submarine landslides. A plane strain model with the slope under water  
 553 is shown in Figure 14. A 20m high slope with slope gradient of 45 degrees is  
 554 placed in a horizontal and vertical structure which was used to be a skaing  
 555 table to apply earthquake loading. We simplify the earthquake loading by  
 556 simulating the ground shaking for 20 seconds with the peak ground acceler-  
 557 ation of 1g and the frequency of 2Hz (Figure 15a). The ground motion is  
 558 applied in terms of velocity (Figure 15b). The earthquake of this magnitude  
 559 can occur typically for the earthquake of magnitude of more than 6.

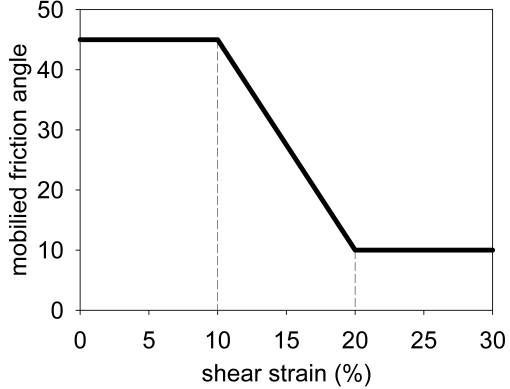


Figure 16: Mobilized friction angle in Mohr Coulomb model

561 A non-associated Mohr-Coulomb model is used for the soil. The soil grain  
 562 has the density of  $2650 \text{ kg/m}^3$ , Young's modulus of 10 kPa and Poisson's  
 563 ratio of 0.3 and zero cohesion. The mobilized friction angle  $\phi'_m$  is governed  
 564 following the softening curve (see Figure 16) with the peak friction angle  $\phi'_p$   
 565 of 45 degrees and the residual friction angle  $\phi'_r$  of 10 degrees. The porosity  
 566 is 0.3 and the average grain size of the soil is around  $0.1 \mu\text{m}$  to mimic the  
 567 undrained behavior. The mobilized dilatancy angle is calculated from the  
 568 Row-stress dilatancy as follow:

$$\sin \psi'_m = \frac{\sin \phi'_m - \sin \phi'_r}{1 - (\sin \phi'_r \sin \phi'_m)} \quad (100)$$

569 The solid plane is modeled as a rigid body acted as a shaking table. The  
 570 contact between horizontal plane and the sand is the frictional contact with  
 571 the friction coefficient of 0.1. No artificial damping is applied in the simu-  
 572 lation. The contact between vertical plane and the sand is considered to be  
 573 smooth with zero friction coefficient. Under gravity, the density of the water  
 574 at the surface is  $999.8 \text{ kg/m}^3$  at the pressure of 1 atm. At the top boundary,  
 575 the air has a density of  $1.17 \text{ kg/m}^3$  at the atmospheric pressure of 1 atm.  
 576 At 5 Celsius degrees, air and water have viscosity of  $18.45e^{-3} \text{ mPa s}$  and 1  
 577 mPa s respectively. On all boundary faces, the symmetric boundary condi-  
 578 tion is imposed, while the Neumann boundary condition is imposed at the  
 579 top boundary for pressure ( $d\rho/dx = 0 \text{ kPa}$ ) and density ( $d\rho/dx = 0 \text{ kg/m}^3$ ).  
 580 The mesh size is  $0.25 \times 0.25 \text{ m}$  with 300852 element cells and 142316 material  
 581 points. The simulation takes a couple of hours to perform 60 seconds of the

582 simulation using 4096 CPUs.

583

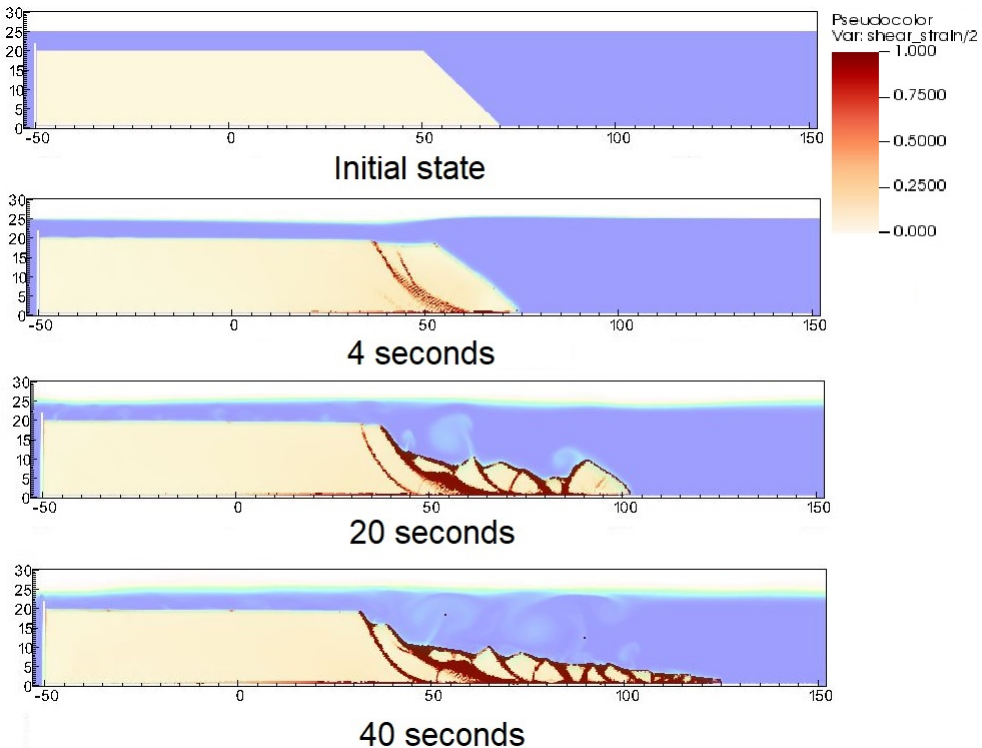
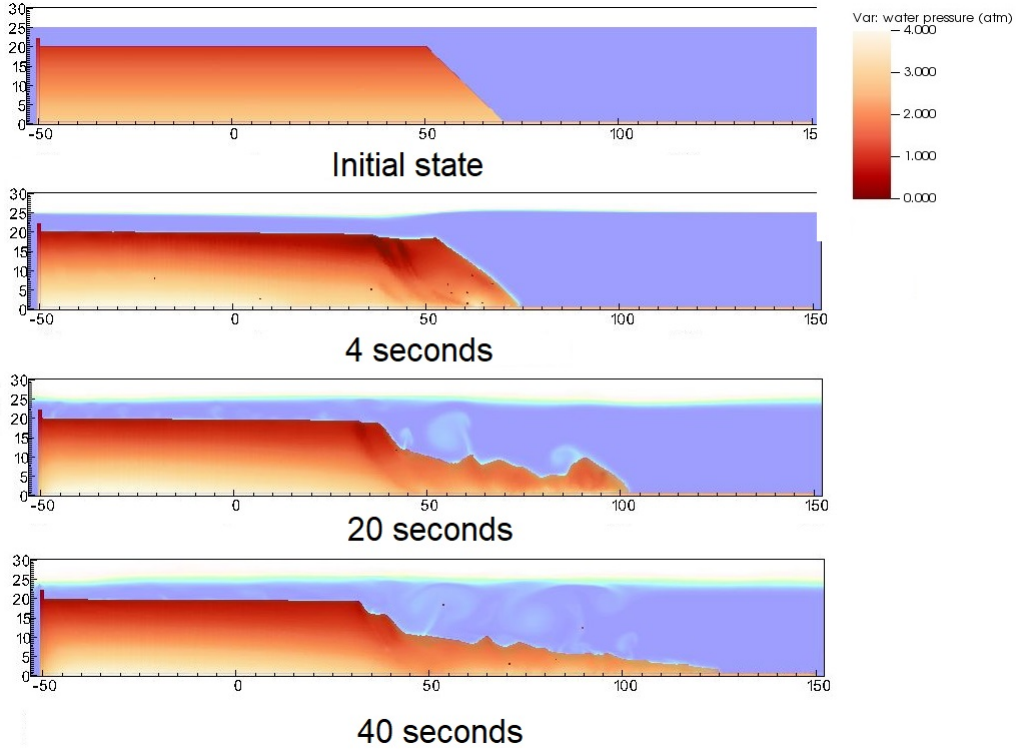


Figure 17: Shear strain during the earthquake-induced submarine landslides

584 We demonstrate the entire process and the mechanism of the earthquake-  
585 induced submarine landslides by showing the shear strain (Figure 17), the  
586 pore water pressure in atm (Figure 18) and the velocity (Figure 19). The  
587 failure mechanism can be characterized as the progressive failure mechanism.  
588 Here are some numerical observation:

589

- 590 1. At the initial of the seismic event, the seismic loading triggers the  
591 first slide at 3 seconds. At 4 seconds, the debris start to move with the  
592 maximum speed of around 2-3 m/s with multiple shear band developed  
593 in the slope. The wave generated from the submarine slide is around  
594 2-3m towards the slide direction.



*Figure 18: pore water pressure during the earthquake-induced submarine landslides*

- 595     2. When the onset of the shear band occurs in the slope (for example  
 596       at 4 seconds and 20 seconds), the negative excess pore water pressure  
 597       is developed along this shear band with pore water pressure is under  
 598       1atm. This is a typical dilatancy behavior when the soil is sheared  
 599       rapidly in the undrained behavior.
- 600     3. When the seismic loading ends at 23 seconds, the last shear band is  
 601       mobilized and the slope soon reaches to the final deposition. No more  
 602       progressive failure developed in the slope. The turbulent flow developed  
 603       as the interaction between debris flow and seawater.
- 604     Overall, we show the completed process of the earthquake-induced submarine  
 605       landslides involving (1) earthquake triggering mechanism, (2) the onset of the  
 606       shear band with the development of negative excess pore water pressure, (3)  
 607       progressive failure mechanism, (4) submarine landslide induced wave to final  
 608       deposition.

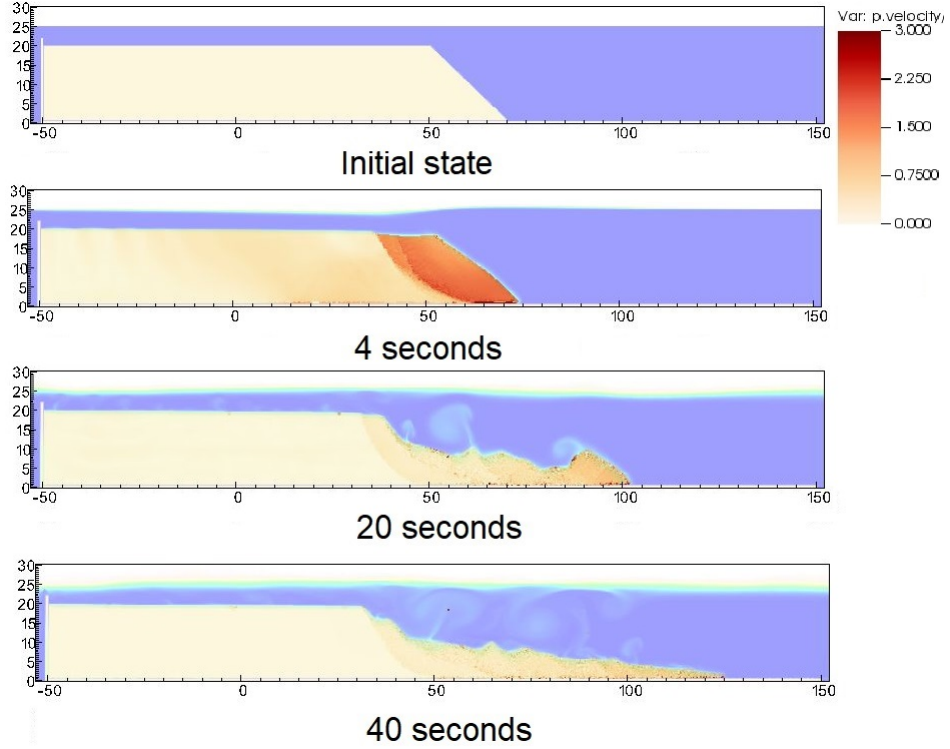


*Figure 19: Velocity during the earthquake-induced submarine landslides*

## 609     **Conclusions**

610     We have presented a numerical approach MPMICE for the simulation  
 611     of large deformation soil-fluid-structure interaction, emphasizing the simu-  
 612     lation of the earthquake-induced submarine landslides. The model uses (1)  
 613     the Material Point Method for capturing the large deformation of iso-thermal  
 614     porous media and solid structures and (2) Implicit Continuous Eulerian (com-  
 615     pressible, conservative multi-material CFD formulation) for modeling the  
 616     complex fluid flow including turbulence. This model is implemented in the  
 617     high-performance Uintah computational framework and validated against an-  
 618     alytical solution and experiment. We then demonstrate the capability of the  
 619     model to simulate the entire process of the earthquake induced submarine  
 620     landslides.

621 **Acknowledgements**

622 The authors gratefully acknowledge Dr. James Guilkey and Dr. Todd  
 623 Harman from the University of Utah for sharing the insight on the theoretical  
 624 framework of MPMICE which this work is based. This project has received  
 625 funding from the European Union's Horizon 2020 research and innovation  
 626 program under the Marie Skłodowska-Curie Actions (MSCA) Individual Fel-  
 627 lowship (Project SUBSLIDE "Submarine landslides and their impacts on  
 628 offshore infrastructures") grant agreement 101022007. The authors would  
 629 also like to acknowledge the support from the Research Council of Norway  
 630 through its Centers of Excellence funding scheme, project number 262644  
 631 Porelab. The computations were performed on High Performance Comput-  
 632 ing resources provided by UNINETT Sigma2 - the National Infrastructure  
 633 for High Performance Computing and Data Storage in Norway.

634 **Appendix: Equation derivation**

635 Before deriving the governing equation, we define the Lagrangian deriva-  
 636 tive for a state variable  $f$  as:

$$\frac{D_f f}{Dt} = \frac{\partial f}{\partial t} + \mathbf{U}_f \cdot \nabla f \quad \frac{D_s f}{Dt} = \frac{\partial f}{\partial t} + \mathbf{U}_s \cdot \nabla f \quad (101)$$

we use some definition following [16] as below:

$$-\frac{1}{V} \left[ \frac{\partial V_f}{\partial p} \right] \equiv \kappa_f \quad \text{isothermal compressibility of fluid} \quad (102)$$

$$\frac{1}{V} \left[ \frac{\partial V_f}{\partial T} \right] \equiv \alpha_f \quad \text{constant pressure thermal expansivity of fluid} \quad (103)$$

637 Then, the rate of volume with incompressible solid grains are calculated as  
 638 below:

$$\frac{1}{V} \frac{D_f V_f}{Dt} = \frac{1}{V} \left( \left[ \frac{\partial V_f}{\partial p} \right] \frac{D_f P_{eq}}{Dt} + \left[ \frac{\partial V_f}{\partial T_f} \right] \frac{D_f T_f}{Dt} \right) = \frac{1}{V} \left( -\kappa_f \frac{D_f P_{eq}}{Dt} + \alpha_f \frac{D_f T_f}{Dt} \right) \quad (104)$$

639 *Evolution of porosity*

640 Solving the solid mass balance equation (4) with the definition of solid  
 641 mass in equation (2), it leads to the rate of porosity as below:

$$\frac{D_s m_s}{Dt} = \frac{D_s (\phi_s \rho_s V)}{Dt} = \rho_s V \frac{D_s \phi_s}{Dt} + \phi_s V \frac{D_s \rho_s}{Dt} + \phi_s \rho_s \frac{D_s V}{Dt} = 0 \quad (105)$$

642 The soil grains are assumed to be incompressible, therefore, term 2 in the  
 643 right hand side is zero.

$$V \frac{D_s \phi_s}{Dt} + \phi_s \frac{D_s V}{Dt} = 0 \quad (106)$$

644 Dividing all terms with  $V$  with the equation  $\frac{1}{V} \frac{D_s V}{Dt} = \nabla \cdot \mathbf{U}_s$ , it leads to:

$$\frac{D_s n}{Dt} = \frac{\partial n}{\partial t} + \mathbf{U}_s \cdot \nabla n = \phi_s \nabla \cdot \mathbf{U}_s \quad (107)$$

645 *Momentum conservation*

646 The linear momentum balance equation for the fluid phases based on  
 647 mixture theory is:

648

$$\frac{1}{V} \frac{D_f(m_f \mathbf{U}_f)}{Dt} = \nabla \cdot (-\phi_f p_f \mathbf{I}) + \nabla \cdot \boldsymbol{\tau}_f + \bar{\rho}_f \mathbf{b} + \sum \mathbf{f}_d + \mathbf{f}_b \quad (108)$$

649 On the right hand sand, the first term is the divergence of partial fluid phase  
 650 stress, the third term is the body force, the fourth term is the drag force  
 651 (momentum exchange) and the fifth term is the buoyant force described in  
 652 [25] for the immiscible mixtures. The buoyant force is in the form:

653

$$\mathbf{f}_b = \boldsymbol{\sigma}_f \nabla(n) \quad (109)$$

654 As a result, the linear momentum balance equation for the fluid phases be-  
 655 comes:

$$\frac{1}{V} \frac{D_f(m_f \mathbf{U}_f)}{Dt} = \frac{1}{V} \left[ \frac{\partial(m_f \mathbf{U}_f)}{\partial t} + \nabla \cdot (m_f \mathbf{U}_f \mathbf{U}_f) \right] = -\phi_f \nabla p_f + \nabla \cdot \boldsymbol{\tau}_f + \bar{\rho}_f \mathbf{b} + \sum \mathbf{f}_d \quad (110)$$

656 The Reynolds stress component can be included in the term  $\boldsymbol{\tau}_f$  to consider the  
 657 turbulent effects if needed. To derive the linear momentum balance equation  
 658 for the solid phase, we begin with the linear momentum balance equation for  
 659 the mixture as:

$$\frac{1}{V} \frac{D_f(m_f \mathbf{U}_f)}{Dt} + \frac{1}{V} \frac{D_s(m_s \mathbf{U}_s)}{Dt} = \nabla \cdot (\boldsymbol{\sigma}) + \bar{\rho}_f \mathbf{b} + \bar{\rho}_s \mathbf{b} \quad (111)$$

660 Combining Terzaghi's equation (3) and subtracting both sides with equation  
 661 (110), we obtain the linear momentum balance equation for the solid phase  
 662 as:

$$\frac{1}{V} \frac{D_s(m_s \mathbf{U}_s)}{Dt} = \nabla \cdot (\boldsymbol{\sigma}') - \phi_s \nabla p_f + \bar{\rho}_s \mathbf{b} - \sum \mathbf{f}_d + \sum \mathbf{f}_{fric} \quad (112)$$

663 Here the  $\mathbf{f}_{fric}$  stems from the soil-structure interaction following the contact  
 664 law between the soil/structure interfaces.

665 *Energy conservation*

666 We adopt the general form of the total energy balance equation for the  
 667 porous media from [26], the total energy balance equations for the fluid phases  
 668 are:

$$\frac{1}{V} \frac{D_f(m_f(e_f + 0.5\mathbf{U}_f^2))}{Dt} = \nabla \cdot (-np_f \mathbf{I}) \cdot \mathbf{U}_f + \nabla \cdot \mathbf{q}_f + (\bar{\rho}_f \mathbf{b}) \cdot \mathbf{U}_f + \sum \mathbf{f}_d \cdot \mathbf{U}_f + \sum q_{sf} \quad (113)$$

669 Applying the product rule  $D(m\mathbf{U}^2) = D(m\mathbf{U} \cdot \mathbf{U}) = 2\mathbf{U} \cdot D(m\mathbf{U})$ , the left  
 670 hand side of equation (113) becomes:

$$\frac{1}{V} \frac{D_f(m_f(e_f + 0.5\mathbf{U}_f^2))}{Dt} = \frac{1}{V} \frac{D_f(m_f e_f)}{Dt} + \frac{1}{V} \frac{D_f(m_f \mathbf{U}_f)}{Dt} \cdot \mathbf{U}_f \quad (114)$$

671 Combining equations (110), (113), (114), we obtain the final form of the  
 672 internal energy balance equation for the fluid phases as:

$$\frac{1}{V} \frac{D_f(m_f e_f)}{Dt} = \frac{1}{V} \left[ \frac{\partial(m_f e_f)}{\partial t} + \nabla \cdot (m_f e_f \mathbf{U}_f) \right] = \bar{\rho}_f p_f \frac{D_f v_f}{Dt} + \nabla \cdot \mathbf{q}_f + \sum q_{sf} \quad (115)$$

673 On the right hand side, the terms include the average pressure-volume work,  
 674 the average viscous dissipation, the thermal transport and the energy ex-  
 675 change between solid and fluid respectively. The heat flux is  $\mathbf{q}_f = \bar{\rho}_f \beta_f \nabla T_f$   
 676 with  $\beta_f$  being the thermal conductivity coefficient. To derive the internal  
 677 energy balance equation for the solid phase, we introduce the rate of the  
 678 internal energy for the thermoelastic materials as a function of elastic strain  
 679 tensor  $\boldsymbol{\epsilon}_s^e$  and temperature  $T_s$ :

$$\frac{m_s}{V} \frac{D_s(e_s)}{Dt} = \boldsymbol{\sigma}' : \frac{D_s(\boldsymbol{\epsilon}_s^e)}{Dt} + \frac{D_s(e_s)}{D_s(T_s)} \frac{D_s(T_s)}{Dt} = \boldsymbol{\sigma}' : \frac{D_s(\boldsymbol{\epsilon}_s^e)}{Dt} + c_v \frac{D_s(T_s)}{Dt} \quad (116)$$

680  $c_v$  is the specific heat at the constant volume of the solid materials. The total  
 681 energy balance equation for the mixture based on [26] can be written as:

$$\begin{aligned} & \frac{1}{V} \frac{D_f(m_f(e_f + 0.5\mathbf{U}_f^2))}{Dt} + \frac{1}{V} \frac{D_s(m_s(e_s + 0.5\mathbf{U}_s^2))}{Dt} = \nabla \cdot (-\phi_f p_f \mathbf{I}) \cdot \mathbf{U}_f \\ & + \nabla \cdot (\boldsymbol{\sigma}' - \phi_s p_f \mathbf{I}) \cdot \mathbf{U}_s + (-\phi_f p_f \mathbf{I}) : \nabla \mathbf{U}_f + \boldsymbol{\sigma}' : \nabla \mathbf{U}_s \\ & + (\bar{\rho}_f \mathbf{b}) \cdot \mathbf{U}_f + (\bar{\rho}_s \mathbf{b}) \cdot \mathbf{U}_s + \nabla \cdot \mathbf{q}_f + \nabla \cdot \mathbf{q}_s + \sum \mathbf{f}_d \cdot (\mathbf{U}_f - \mathbf{U}_s) \end{aligned} \quad (117)$$

684 Subtracting equation (117), (116) to equations (113) and (112), we obtained  
 685 the internal energy balance equation for solid phase as:

$$\boldsymbol{\sigma}' : \frac{D_s(\epsilon_s^e)}{Dt} + \frac{m_s}{V} c_v \frac{D_s(T_s)}{Dt} = \Delta W_s + \Delta W_{friction} + \nabla \cdot \mathbf{q}_s - \sum q_{sf} \quad (118)$$

686 On the right hand side, the terms include the work rate from frictional sliding  
 687 between solid materials  $\Delta W_{friction}$ , thermal transport and energy exchange  
 688 between solid and fluid respectively. The heat flux is  $\mathbf{q}_s = \bar{\rho}_s \beta_s \nabla T_s$  with  $\beta_s$   
 689 being the thermal conductivity of the solid materials, the mechanical work  
 690 rate  $\Delta W_s = \boldsymbol{\sigma}' : \frac{D_s(\epsilon_s)}{Dt} = \boldsymbol{\sigma}' : (\frac{D_s(\epsilon_s^e)}{Dt} + \frac{D_s(\epsilon_s^p)}{Dt})$  computed from the constitutive  
 691 model with  $\epsilon_s^p$  is the plastic strain tensor, . By subtracting the term  $\boldsymbol{\sigma}' : \frac{D_s(\epsilon_s^e)}{Dt}$ ,  
 692 we get the final form of the energy balance equation as:

$$\frac{m_s}{V} c_v \frac{D_s(T_s)}{Dt} = \boldsymbol{\sigma}' : \frac{D_s(\epsilon_s^p)}{Dt} + \Delta W_{friction} + \nabla \cdot \mathbf{q}_s - \sum q_{sf} \quad (119)$$

### 693 Advanced Fluid Pressure

694 The discretization of the pressure equation begins with the Lagrangian  
 695 face-centered velocity and the equation for the pressure

$$\bar{\rho}_{f,FC} \frac{\mathbf{U}_{f,FC}^{n+1} - \mathbf{U}_{f,FC}^n}{dt} = n \nabla^{FC} P_{fc}^{n+1} + \bar{\rho}_{f,FC} \mathbf{b} \quad (120)$$

696

$$\kappa \frac{dP}{dt} = \nabla^c \cdot \mathbf{U}_{f,FC}^{n+1} \quad (121)$$

697 The divergence of the equation (120) with  $\nabla \cdot \mathbf{b} = 0$  is

$$\nabla^c \cdot \mathbf{U}_{f,FC}^{n+1} - \nabla^c \cdot \mathbf{U}_{f,FC}^n = \nabla^c \frac{\Delta t}{\rho_{f,FC}^n} \cdot \nabla^{FC} (P_{fc}^n + \Delta P_{fc}^n) \quad (122)$$

698 To solve this equation, we define the face-centered intermediate velocity  
 699  $\mathbf{U}_{f,FC}^*$  as:

$$\bar{\rho}_{f,FC} \frac{\mathbf{U}_{f,FC}^* - \mathbf{U}_{f,FC}^n}{\Delta t} = n \nabla^{FC} P_{fc}^n + \bar{\rho}_{f,FC} \mathbf{b} \quad (123)$$

700 The divergence of the equation (123) is

$$\nabla^c \cdot \mathbf{U}_{f,FC}^* - \nabla^c \cdot \mathbf{U}_{f,FC}^n = \nabla^c \frac{\Delta t}{\rho_{f,FC}^n} \cdot \nabla^{FC} P_{fc}^n \quad (124)$$

701 Combining equations (121, 122, 124), it leads to

$$\left( \kappa - \nabla^c \frac{\Delta t}{\rho_{f,FC}^n} \cdot \nabla^{FC} \right) \Delta P_{fc}^n = -\nabla^c \cdot \mathbf{U}_{f,FC}^* \quad (125)$$

702 When the fluid is incompressible,  $\kappa$  approaches to zero and the equation  
703 (125) becomes the Poisson's equation for the incompressible fluid flow.

704 *Momentum and Energy exchange with an implicit solver*

705 Considering the fluid momentum balance equation as

$$(m\mathbf{U})_{f,FC}^{n+1} = (m\mathbf{U})_{f,FC}^n - \Delta t(Vn\nabla^{FC}P_{fc}^n + m_f\mathbf{b}) + VK\Delta t(\mathbf{U}_{s,FC}^{n+1} - \mathbf{U}_{f,FC}^{n+1}) \quad (126)$$

706 Assuming  $m_{f,FC}^{n+1} = m_{f,FC}^n$  we get

$$\mathbf{U}_{f,FC}^{n+1} = \mathbf{U}_{f,FC}^n - \Delta t\left(\frac{\nabla^{FC}P_{fc}^n}{\rho_{f,FC}^n} + \mathbf{b}\right) + \frac{\Delta tK}{\bar{\rho}_{f,FC}^n}(\mathbf{U}_{s,FC}^{n+1} - \mathbf{U}_{f,FC}^{n+1}) \quad (127)$$

707 As defined in the section 'Advanced Fluid Pressure', the face-centered inter-  
708 mediate fluid velocity  $\mathbf{U}_{f,FC}^* = \Delta t(\nabla^{FC}P_{fc}^n/\rho_{f,FC}^n + \mathbf{b})$  leading to

$$\mathbf{U}_{f,FC}^{n+1} = \mathbf{U}_{f,FC}^* + \frac{\Delta tK}{\bar{\rho}_{f,FC}^n}(\mathbf{U}_{s,FC}^{n+1} - \mathbf{U}_{f,FC}^{n+1}) \quad (128)$$

709 Considering the solid momentum balance equation as

$$(m\mathbf{U})_{s,FC}^{n+1} = (m\mathbf{U})_{s,FC}^n - \Delta t(V\nabla^{FC} \cdot \boldsymbol{\sigma}'^n - V(1-n)\nabla^{FC}P_{fc}^n + m_s\mathbf{b}) - VK\Delta t(\mathbf{U}_{s,FC}^{n+1} - \mathbf{U}_{f,FC}^{n+1}) \quad (129)$$

710 We define the face-centered intermediate solid velocity as  $\mathbf{U}_{s,FC}^* = \Delta t(\nabla^{FC} \cdot \boldsymbol{\sigma}'^n / \bar{\rho}_{s,FC}^n - \nabla^{FC}P_{fc}^n/\rho_s + \mathbf{b})$  leading to

$$\mathbf{U}_{s,FC}^{n+1} = \mathbf{U}_{s,FC}^* - \frac{\Delta tK}{\bar{\rho}_{s,FC}^n}(\mathbf{U}_{s,FC}^{n+1} - \mathbf{U}_{f,FC}^{n+1}) \quad (130)$$

712 Combining equation (128) and (130) we get

$$\begin{aligned} \mathbf{U}_{f,FC}^* + \Delta\mathbf{U}_{f,FC} &= \mathbf{U}_{f,FC}^* + \frac{\Delta tK}{\bar{\rho}_{f,FC}^n}(\mathbf{U}_{s,FC}^* + \Delta\mathbf{U}_{s,FC} - \mathbf{U}_{f,FC}^* - \Delta\mathbf{U}_{f,FC}) \\ \mathbf{U}_{s,FC}^* + \Delta\mathbf{U}_{s,FC} &= \mathbf{U}_{s,FC}^* - \frac{\Delta tK}{\bar{\rho}_{s,FC}^n}(\mathbf{U}_{s,FC}^* + \Delta\mathbf{U}_{s,FC} - \mathbf{U}_{f,FC}^* - \Delta\mathbf{U}_{f,FC}) \end{aligned} \quad (131)$$

713 Rearranging the equation (131), it leads to the linear system of equations

$$\begin{vmatrix} (1 + \beta_{12,FC}) & -\beta_{12,FC} \\ -\beta_{21,FC} & (1 + \beta_{21,FC}) \end{vmatrix} \begin{vmatrix} \Delta \mathbf{U}_{f,FC} \\ \Delta \mathbf{U}_{s,FC} \end{vmatrix} = \begin{vmatrix} \beta_{12,FC}(\mathbf{U}_{s,FC}^* - \mathbf{U}_{f,FC}^*) \\ \beta_{21,FC}(\mathbf{U}_{f,FC}^* - \mathbf{U}_{s,FC}^*) \end{vmatrix}$$

714 Solving this linear equations with  $\beta_{12,FC} = (\Delta t K) / \bar{\rho}_{f,FC}^n$  and  $\beta_{21,FC} =$   
 715  $(\Delta t K) / \bar{\rho}_{s,FC}^n$  with K is the momentum exchange coefficient. Similar derivation  
 716 can be performed to computed the cell-center velocity increment leading  
 717 to

$$\begin{vmatrix} (1 + \beta_{12c}) & -\beta_{12c} \\ -\beta_{21c} & (1 + \beta_{21c}) \end{vmatrix} \begin{vmatrix} \Delta \mathbf{U}_{fc} \\ \Delta \mathbf{U}_{sc} \end{vmatrix} = \begin{vmatrix} \beta_{12c}(\mathbf{U}_{sc}^* - \mathbf{U}_{fc}^*) \\ \beta_{21c}(\mathbf{U}_{fc}^* - \mathbf{U}_{sc}^*) \end{vmatrix}$$

718 with  $\beta_{12c} = (\Delta t K) / \bar{\rho}_{fc}^n$  and  $\beta_{21c} = (\Delta t K) / \bar{\rho}_{sc}^n$  and the cell-centered interme-  
 719 diate velocity can be calculated by

$$\begin{aligned} \mathbf{U}_{fc}^* &= \mathbf{U}_{fc}^n + \Delta t \left( -\frac{\nabla P_{fc}^{n+1}}{\rho_{fc}^n} + \frac{\nabla \cdot \boldsymbol{\tau}_{fc}^n}{\bar{\rho}_{fc}^n} + \mathbf{b} \right) \\ \mathbf{U}_{sc}^* &= \mathbf{U}_{sc}^n + \Delta t \left( \frac{\nabla \cdot \boldsymbol{\sigma}_c'^n}{\bar{\rho}_{sc}^n} - \frac{\nabla P_{sc}^{n+1}}{\rho_s} + \mathbf{b} \right) \end{aligned} \quad (132)$$

720 For generalize multi materials i,j = 1:N, the linear equations is in the form:

$$\begin{vmatrix} (1 + \beta_{ij}) & -\beta_{ij} \\ -\beta_{ji} & (1 + \beta_{ji}) \end{vmatrix} \begin{vmatrix} \Delta \mathbf{U}_i \\ \Delta \mathbf{U}_j \end{vmatrix} = \begin{vmatrix} \beta_{ij}(\mathbf{U}_i^* - \mathbf{U}_j^*) \\ \beta_{ji}(\mathbf{U}_j^* - \mathbf{U}_i^*) \end{vmatrix}$$

721 Similar approach applied for the energy exchange term leading to:

$$\begin{vmatrix} (1 + \eta_{ij}) & -\eta_{ij} \\ -\eta_{ji} & (1 + \eta_{ji}) \end{vmatrix} \begin{vmatrix} \Delta T_i \\ \Delta T_j \end{vmatrix} = \begin{vmatrix} \eta_{ij}(T_i^n - T_j^n) \\ \eta_{ji}(T_j^n - T_i^n) \end{vmatrix}$$

722 with  $\eta$  is the energy exchange coefficient.

## 723 References

- 724 [1] D. Yuk, S. Yim, P.-F. Liu, Numerical modeling of submarine mass-  
 725 movement generated waves using RANS model, Computers and Geo-  
 726 sciences 32 (7) (2006) 927–935. doi:10.1016/j.cageo.2005.10.028.  
 727 URL <https://doi.org/10.1016/j.cageo.2005.10.028>

- 728 [2] S. Glimsdal, J.-S. L'Heureux, C. B. Harbitz, F. Løvholt, The 29th january 2014 submarine landslide at statland, norway—landslide dynamics,  
729 tsunami generation, and run-up, *Landslides* 13 (6) (2016) 1435–1444.  
730 doi:10.1007/s10346-016-0758-7.  
731 URL <https://doi.org/10.1007/s10346-016-0758-7>
- 733 [3] S. Abadie, D. Morichon, S. Grilli, S. Glockner, Numerical simulation  
734 of waves generated by landslides using a multiple-fluid  
735 navier–stokes model, *Coastal Engineering* 57 (9) (2010) 779–794.  
736 doi:10.1016/j.coastaleng.2010.03.003.  
737 URL <https://doi.org/10.1016/j.coastaleng.2010.03.003>
- 738 [4] M. Rauter, S. Viroulet, S. S. Gylfadóttir, W. Fellin, F. Løvholt, Granular  
739 porous landslide tsunami modelling – the 2014 lake askja flank collapse,  
740 *Nature Communications* 13 (1) (Feb. 2022). doi:10.1038/s41467-022-  
741 28296-7.  
742 URL <https://doi.org/10.1038/s41467-022-28296-7>
- 743 [5] Q.-A. Tran, W. Sołowski, Generalized interpolation material point  
744 method modelling of large deformation problems including strain-  
745 rate effects – application to penetration and progressive failure  
746 problems, *Computers and Geotechnics* 106 (2019) 249–265.  
747 doi:10.1016/j.compgeo.2018.10.020.  
748 URL <https://doi.org/10.1016/j.compgeo.2018.10.020>
- 749 [6] T. Capone, A. Panizzo, J. J. Monaghan, SPH modelling of water  
750 waves generated by submarine landslides, *Journal of Hydraulic Research*  
751 48 (sup1) (2010) 80–84. doi:10.1080/00221686.2010.9641248.  
752 URL <https://doi.org/10.1080/00221686.2010.9641248>
- 753 [7] X. Zhang, E. Oñate, S. A. G. Torres, J. Bleyer, K. Krabbenhoft, A  
754 unified lagrangian formulation for solid and fluid dynamics and its possi-  
755 bility for modelling submarine landslides and their consequences, *Computer  
756 Methods in Applied Mechanics and Engineering* 343 (2019) 314–  
757 338. doi:10.1016/j.cma.2018.07.043.  
758 URL <https://doi.org/10.1016/j.cma.2018.07.043>
- 759 [8] R. Dey, B. C. Hawlader, R. Phillips, K. Soga, Numerical modelling  
760 of submarine landslides with sensitive clay layers, *Géotechnique* 66 (6)

- 761 (2016) 454–468. doi:10.1680/jgeot.15.p.111.  
762 URL <https://doi.org/10.1680/jgeot.15.p.111>
- 763 [9] S. Bandara, K. Soga, Coupling of soil deformation and pore fluid flow  
764 using material point method, Computers and Geotechnics 63 (2015)  
765 199–214. doi:10.1016/j.compgeo.2014.09.009.  
766 URL <https://doi.org/10.1016/j.compgeo.2014.09.009>
- 767 [10] A. P. Tampubolon, T. Gast, G. Klár, C. Fu, J. Teran, C. Jiang,  
768 K. Museth, Multi-species simulation of porous sand and water  
769 mixtures, ACM Transactions on Graphics 36 (4) (2017) 1–11.  
770 doi:10.1145/3072959.3073651.  
771 URL <https://doi.org/10.1145/3072959.3073651>
- 772 [11] A. S. Baumgarten, K. Kamrin, A general constitutive model for dense,  
773 fine-particle suspensions validated in many geometries, Proceedings  
774 of the National Academy of Sciences 116 (42) (2019) 20828–20836.  
775 doi:10.1073/pnas.1908065116.  
776 URL <https://doi.org/10.1073/pnas.1908065116>
- 777 [12] Q.-A. Tran, W. Sołowski, Temporal and null-space filter for the ma-  
778 terial point method, International Journal for Numerical Methods in  
779 Engineering 120 (3) (2019) 328–360. doi:10.1002/nme.6138.  
780 URL <https://doi.org/10.1002/nme.6138>
- 781 [13] X. Zheng, F. Pisanò, P. J. Vardon, M. A. Hicks, An explicit stabilised  
782 material point method for coupled hydromechanical problems in two-  
783 phase porous media, Computers and Geotechnics 135 (2021) 104112.  
784 doi:10.1016/j.compgeo.2021.104112.  
785 URL <https://doi.org/10.1016/j.compgeo.2021.104112>
- 786 [14] Q. A. Tran, W. Sołowski, M. Berzins, J. Guilkey, A convected particle  
787 least square interpolation material point method, International Jour-  
788 nal for Numerical Methods in Engineering 121 (6) (2019) 1068–1100.  
789 doi:10.1002/nme.6257.  
790 URL <https://doi.org/10.1002/nme.6257>
- 791 [15] J.-S. Chen, M. Hillman, S.-W. Chi, Meshfree methods: Progress made  
792 after 20 years, Journal of Engineering Mechanics 143 (4) (Apr. 2017).

- 793                   doi:10.1061/(asce)em.1943-7889.0001176.  
 794                   URL [https://doi.org/10.1061/\(asce\)em.1943-7889.0001176](https://doi.org/10.1061/(asce)em.1943-7889.0001176)
- 795 [16] B. A. Kashiwa, A multifield model and method for fluid-structure in-  
 796 teraction dynamics, Tech. Rep. LA-UR-01-1136, Los Alamos National  
 797 Laboratory (2001).
- 798 [17] J. Guilkey, T. Harman, B. Banerjee, An eulerian-lagrangian  
 799 approach for simulating explosions of energetic devices,  
 800 Computers and Structures 85 (11) (2007) 660 – 674.  
 801 doi:<https://doi.org/10.1016/j.compstruc.2007.01.031>.  
 802 URL <http://www.sciencedirect.com/science/article/pii/S0045794907000429>
- 803 [18] A. S. Baumgarten, B. L. Couchman, K. Kamrin, A coupled finite volume  
 804 and material point method for two-phase simulation of liquid-sediment  
 805 and gas-sediment flows, Computer Methods in Applied Mechanics and  
 806 Engineering 384 (2021) 113940. doi:10.1016/j.cma.2021.113940.  
 807 URL <https://doi.org/10.1016/j.cma.2021.113940>
- 808 [19] S. Bardenhagen, J. Guilkey, K. Roessig, J. Brackbill, W. Witzel,  
 809 J.C.Foster, An improved contact algorithm for the material point  
 810 method and application to stress propagation in granular material,  
 811 CMES-Computer Modeling in Engineering and Sciences 2 (2001) 509–  
 812 522. doi:10.3970/cmes.2001.002.509.
- 813 [20] J. A. M. K. R. Beetstra, M. A. van der Hoef, Drag force of intermediate  
 814 reynolds number flow past mono- and bidisperse arrays of spheres,  
 815 Fluid Mechanics and Transport Phenomena 53 (2) (2007) 489 – 501.  
 816 doi:<https://doi.org/10.1002/aic.11065>.
- 817 [21] R. W. Stewart, The air-sea momentum exchange, Boundary-Layer Me-  
 818 teorology 6 (1-2) (1974) 151–167. doi:10.1007/bf00232481.  
 819 URL <https://doi.org/10.1007/bf00232481>
- 820 [22] S. G. B. and E. M. Kober, The generalized interpolation material point  
 821 method, Computer Modeling in Engineering and Sciences 5 (2004) 477–  
 822 496. doi:10.1016/j.compgeo.2021.104199.  
 823 URL <https://doi.org/10.3970/cmes.2004.005.477>
- 824 [23] S. G. Amiri, E. Taheri, A. Lavasan, A hybrid finite element model for  
 825 non-isothermal two-phase flow in deformable porous media, Computers

- 826 and Geotechnics 135 (2021) 104199. doi:10.1016/j.compgeo.2021.104199.  
827 URL <https://doi.org/10.1016/j.compgeo.2021.104199>
- 828 [24] S. A. R. C. Mariotti;, P. Heinrich, Numerical simulation of sub-  
829 marine landslides and their hydraulic effects, Journal of Waterway, Port, Coastal, and Ocean Engineering 123 (4) (1997).  
830 doi:[https://doi.org/10.1061/\(ASCE\)0733-950X\(1997\)123:4\(149\)](https://doi.org/10.1061/(ASCE)0733-950X(1997)123:4(149)).
- 832 [25] D. Drumheller, On theories for reacting immiscible mixtures, International Journal of Engineering Science 38 (3) (2000) 347 – 382.  
833 doi:[https://doi.org/10.1016/S0020-7225\(99\)00047-6](https://doi.org/10.1016/S0020-7225(99)00047-6).  
834 URL <http://www.sciencedirect.com/science/article/pii/S0020722599000476>
- 836 [26] S. Hassanzadeh, Derivation of basic equations of mass transport in  
837 porous media, part1: Macroscopic balance laws, Advances in Water Resources 9 (1986) 196–206. doi:[https://doi.org/10.1016/0309-1708\(86\)90024-2](https://doi.org/10.1016/0309-1708(86)90024-2).  
838  
839